Natural iron fertilization by shallow hydrothermal sources fuels diazotroph blooms in the Ocean

Authors: Sophie Bonnet[1], Cécile Guieu[2], Vincent Taillandier[2], Cédric Boulart[3], Pascale Bouruet-Aubertot[4], Frédéric Gazeau[2], Carla Scalabrin[5], Matthieu Bressac[2], Angela N. Knapp[6], Yannis Cuypers[4], David González-Santana[7,8], Heather J. Forrer[6], Jean-Michel Grisoni[9], Olivier Grosso[1], Jérémie Habasque[7], Mercedes Jardin-Camps[1], Nathalie Leblond[2], Frédéric Le Moigne[1,7], Anne Lebourges-Dhaussy[7], Caroline Lory[1], Sandra Nunige[1], Elvira Pulido-Villena[1], Andrea L. Rizzo[10], Géraldine Sarthou[7], Chloé Tilliette[2]

Affiliations:
[1]Aix Marseille University, Université de Toulon, CNRS, IRD, MIO UM 110, 13288 Marseille, France
[2]Laboratoire d'Océanographie de Villefranche, Institut de la Mer de Villefranche, CNRS, Sorbonne Université, 06230 Villefranche-sur-Mer, France
[3]Adaptation et Diversité en Milieu Marin, UMR 7144 AD2M CNRS-Sorbonne Université, Station Biologique de Roscoff, 29680 Roscoff, France
[4]Laboratoire d'Océanographie et du Climat: Expérimentation et Approches Numériques (LOCEAN-IPSL), Sorbonne University, CNRS-IRD-MNHN, 75005 Paris, France
[5]Ifremer, Univ Brest, CNRS, UMR 6538 Geo-Ocean, F-29280 Plouzané, France
[6]Florida State University, Department of Earth, Ocean, and Atmospheric Sciences, Tallahassee, Florida, 32306, USA
[7]CNRS, Univ Brest, IRD, Ifremer, UMR 6539, LEMAR, Plouzane, France
[8]Instituto de Oceanografía y Cambio Global, IOCAG, Universidad de Las Palmas de Gran Canaria, 35017
[9]Institut de la Mer de Villefranche, IMEV, Sorbonne Université, Villefranche sur Mer
[10]Istituto Nazionale di Geofisica e Vulcanologia, Sezione di Palermo, Via Ugo La Malfa 153, 90146 Palermo, Italy

***Correspondence to:** sophie.bonnet@mio.osupytheas.fr, cecile.guieu@imev-mer.fr

Abstract. Iron is an essential nutrient, regulating productivity in ~30% of the ocean. Compared to deep (>2000 m) hydrothermal activity at mid-ocean ridges that provide iron to the ocean's interior, shallow (<500 m) hydrothermal fluids are likely to influence the surface's ecosystem. However, their effect is unknown. Here we show that fluids emitted along the Tonga volcanic arc (South Pacific) have a dramatic impact on iron concentrations in the photic layer through vertical diffusion. This enrichment stimulates biological activity, resulting in an extensive patch of chlorophyll. Diazotroph activity is 2-8 times higher, and carbon export fluxes 2-3 times, compared to adjacent unfertilized waters. Such findings reveal a novel mechanism of natural iron fertilization in the ocean, fueling regional hot spot sinks for atmospheric CO_2.

One-Sentence Summary: Shallow hydrothermal iron fertilizes the overlying surface ocean creating an oasis in the desert

Planktonic diazotrophs are microscopic organisms ubiquitous in the ocean, that play a crucial role: they supply new available nitrogen (N) to the surface ocean biosphere, an essential but scarce nutrient in most of our oceans *(1, 2)*. Diazotrophs do so by converting atmospheric N_2 (endlessly available but metabolically useless) to ammonia (readily bioavailable), a reaction termed biological N_2 fixation. Diazotrophs thus alleviate N limitation in 60% of our oceans, especially in low latitudes, promoting CO_2 fixation by phytoplankton into organic carbon (primary productivity), that in turn, sustains the food web and organic carbon export and sequestration to the deep ocean (*3-6*). However, diazotrophs face a major challenge: besides phosphorus requirements, the iron (Fe)-rich nitrogenase enzyme that catalyzes N_2 fixation imposes a high Fe demand on diazotroph growth *(7)*, however Fe bioavailability in the ocean often limits the growth of these organisms *(6, 8)*. The Western subtropical South Pacific (WTSP) is a recognized hotspot of N_2 fixation activity, with an estimated contribution of ~21% to the global fixed N input *(9)*. Fe supply through atmospheric deposition is known to control large-scale diazotroph biogeography *(10)*, but such aeolian inputs are extremely low in this remote region *(11)*, suggesting the presence of alternative Fe fertilization processes underlying the ecological success of diazotrophs. Identifying these processes is of the utmost importance as diazotrophs have recently been identified as key drivers of future marine net primary productivity in response to climate change *(12)*. Here we demonstrate that Fe-rich fluids emitted by shallow hydrothermal venting directly fertilize the overlying surface ecosystem, inducing intense diazotroph activity supporting enhanced carbon export fluxes, with a C sequestration efficiency higher than those from artificial mesoscale Fe-addition experiments.

The WTSP hosts the Tonga-Kermadec subduction zone, stretching 2,500 km from New Zealand to Tonga (Fig. 1A). It is the fastest converging, most seismically active subduction zone, with the highest density of underwater volcanic centers on Earth *(13)*. This system produces extensive plumes of ^3He in the bathypelagic ocean (1500-2000 m) that fingerprint deep hydrothermal sources originating in the Lau basin *(14, 15)*. Other authors *(16, 17)* also identified shallower sources (<500 m) along the Tonga arc, associated with significantly elevated dissolved Fe (DFe) and manganese (DMn) concentrations close to the seafloor. Guieu et al. *(11)* demonstrated that these shallow sources were able to bring DFe up to the photic layer (~100 m) at high concentrations (up to 66 nmol liter^{-1}). These Fe infusions are hypothesized to fuel the observed N_2 fixation hot spot associated with an elevated chlorophyll (Chl) patch persisting 6 months per year in this region *(9, 11)* (Fig 2A,B). Yet, there is currently no empirical evidence of the direct effect of such hydrothermal Fe fertilization on the overlying planktonic ecosystem, with the implication that a significant part of new N entering the tropical Pacific -thanks to hydrothermal Fe- is likely missing from N budgets. Such an Fe supply mechanism would challenge the prevailing paradigm that diazotroph productivity is mainly mediated by Fe from dust deposition *(10)* in N-limited regions.

To document the mechanistic link between Fe supply from submarine volcanism and the response of the surface plankton community, we combine acoustic, chemical, physical, and biological data acquired during the GEOTRACES GPpr14 TONGA expedition *(18),* a zonal transect between the Tonga volcanic arc and the South Pacific Gyre, which serves as a reference deep-sea site where the ocean surface is not impacted by hydrothermal activity. The targeted submarine volcano (Volcano #1 *(16, 17)*) is a large stratovolcano (basal diameter 28 km) located in the central part of the Tonga arc (-21.154 ; -175.744) (Fig. 1A, B). During an acoustic survey above the volcano, we detected multiple acoustic plumes (Fig. 1B, Table S1) rising from the sea floor up to ~20 m below the surface ocean (Fig. 1C). We focused our study on a site located near the caldera on the southwestern edge of the volcano (Fig. 1B) (hereafter referred

to as 'Panamax site'), where the acoustic anomaly *(19-21)*, also associated with intense gas bubble emissions, was strong and continuous (Fig. 1D). Repeated CTD casts at this site revealed that acoustic plumes were also associated with strong anomalies in pH, turbidity, and redox potential (Eh) (Fig. 1E, Table S2) from the seafloor (195 m depth) up to ~160 m. Methane concentrations that reached >100 nmol liter^{-1} (Fig. 1F) and the excess of ^{3}He and ^{4}He concentrations (Fig. S1) confirmed the hydrothermal origin of the plumes.

DFe and DMn were also enriched ~80-fold at this site (Fig. 1F) compared to similar depths in the WTSP *(11, 22)*. DFe and CH_4 concentrations were positively correlated (R^2=0.89, $p<0.05$). DFe reached concentrations as high as 48.5 nmol liter^{-1} at 195 m (within the main acoustic signal), and although they decreased towards the photic layer (~0-100 m), DFe concentrations in that layer (~0.6 to 10 nmol liter^{-1}) (Fig. 1F) were one order of magnitude higher compared to those at stations not impacted by hydrothermal activity *(23)*. The turbulence profiles (Fig. S2) revealed an order of magnitude higher vertical diffusivity above the volcano (Kz = 3.7±1.9x10^{-5} m^2 s^{-1} at ~50 m, corresponding to the base of the surface mixed layer) compared to the distal open-sea reference site (Kz = 5.2±9.6x10^{-6} m^2 s^{-1}) (Table 1), in line with previous work above shallow (~200 m) seamounts (*24*). Combining the measured Kz with the DFe gradients (Table 1 and Supplementary materials), the diffusive DFe vertical supply to the mixed layer above the volcano reached 1.1±1.7x10^{-4} mmol Fe m^{-2} d^{-1}. This is orders of magnitude larger than at the reference site (Table 1), suggesting that Fe-rich fluids released close to the shallow volcano represent a significant Fe source to surface waters. A phosphate supply of 5.4±2.4x10^{-3} mmol m^{-2} d^{-1} accompanied this vertical DFe supply, while no nitrate supply could be quantified (Table S4) due to the decoupling between the depth of the phosphacline (~50 m) and the nitracline (~100 m) (Fig. S5), as already observed in the WTSP (*25*).

Along the west to east zonal transect, total chlorophyll-a (Chl*a)* and particulate organic N stocks peaked in the naturally Fe-fertilized waters at Volcano #1 (Fig. 2). Both were also elevated up and downstream of the arc (Fig. 2C) consistent with ocean color images (Fig. 2A). This biomass peak was associated with 2 to 8-fold enhanced N_2 fixation rates relative to surrounding waters on either side of the arc ($p<0.05$, Mann-Whitney test) (Fig 2E), and 90-fold higher *Trichodesmium* spp. abundances ($p<0.05$, Mann-Whitney test) (Fig. 2F). This led to extremely high N_2 fixation rates and *Trichodesmium* spp. abundances in the Fe-fertilized waters (>2000 µmol N m^{-2} d^{-1} ; ~6 x 10^7 *nifH* copies L^{-1}), i.e. one to two orders of magnitude greater than values commonly found in other (sub)tropical ocean basins (*26*). This peak in diazotroph activity was marked by a phosphate drawdown (~50 nM) in the photic layer, although concentrations were not limiting for *Trichodesmium* spp. *(27)* due to intense microbial phosphorus cycling in this region *(28)*. Diazotrophs were favored by the extremely low nitrate concentrations along the transect (Fig. S6).

The particulate organic carbon (POC) and nitrogen (PON) export fluxes were measured using surface tethered sediment traps deployed for 4 days near Volcano #1 and at the reference site. Consistent with model simulations in this region *(22)*, POC export at 170 m and 270 m was 2 to 3 times higher in the Fe-fertilized patch than at the reference site (Table 1), resulting in an excess of POC export of 1.5 to 2.5 mmol C m^{-2} d^{-1} in the fertilized waters. Comparing measurements of subsurface water column nitrate+nitrite δ^{15}N (1.2 to 2.2‰) with the δ^{15}N of sinking PON (-0.5± 3.5‰ at 170 m and -0.2± 1.9‰ at 270 m, respectively), the N isotope budget (N_2 fixation end member = -1‰) revealed that N_2 fixation supported 77 to 84±159% at 170 m and 64 to 75±86% at 270 m of the export production in the Fe-fertilized area, consistent with the massive export of diazotrophs observed in the traps during the expedition *(3, 29)*. Collectively, these results suggest that the hydrothermally-driven Fe fertilization fuels

planktonic diazotrophs, resulting in low $\delta^{15}N$ of sinking PON and high POC export fluxes compared to subtropical systems not impacted by hydrothermal activity *(30)* (Table S5).

To confirm the causal link between hydrothermal inputs and diazotroph activity, we conducted novel experiments where hydrothermally-enriched waters collected at the 'Panamax site' of Volcano #1 (hereafter referred to as 'plume water') were supplied to surface biological communities using 300-L trace metal clean reactors (Fig. S7A, Methods). Increasing plume water volumes (from 0 to 14.5% of the total reactors volume) were added to surface seawater from outside of the direct volcanic influence (-21.683°N ; -174.709°E). The plume water was characterized by low pH (6.4) compared to ambient seawater (8.1) and DFe concentrations (15.8 nmol liter^{-1}) were ~15-fold higher than in ambient surface waters (1.0 nmol liter^{-1}) (Table S6). The increasing additions resulted in consistent increases of DFe concentrations and decreasing pH in the experimental reactors (Fig. S7). Plume water additions enhanced N_2 fixation rates by a factor of 7 to 8 on average over all sampling days compared to those measured in the unamended control ($p<0.05$, Mann-Whitney test) (Fig. 3A), reaching levels in the same range as *in situ* rates measured above the volcano (Fig. 2E). Likewise, as observed *in-situ*, *Trichodesmium* abundances increased by a factor of 3 to 5-fold ($p<0.05$, Mann-Whitney test) in plume water-amended reactors (Fig. 3B). Both N_2 fixation rates and *Trichodesmium* abundances decreased at the end of the experiment, likely as a consequence of phosphate depletion in the closed reactors (no possible turbulent diffusion) (Fig. S7), but generally remained higher in the amended reactors compared to those measured in the control. Due to the low inorganic N:P molar ratio (~9:1) in the plume water (indicative of a greater phosphate availability relative to nitrate), the mixing of the plume water with surface seawater likely prevented the phosphate limitation for up to days 6-8, while nitrate was depleted after 2 days. This decoupling between nitrate and phosphate also mirrors the *in situ* data described above.

The Fe supply from the Tonga arc thus drives in large part upper ocean phenology of biological activity. We estimate that the region of elevated Chl*a* extends ~800 km in longitude and ~450 km in latitude (Fig. 1A), forming a hot spot of biological activity of ~360,000 km^2 in the middle of the otherwise desert-like WTSP. The trajectories of SVP (surface velocity program) drifters deployed above Volcano #1 indicate that over a 6-month period, Fe-fertilized water masses can be dispersed regionally and support this extended Chl*a* patch (Fig. S8). The trajectories provide a bulk representation of complex dynamical processes occurring at smaller scales, involving the South Equatorial current and modulated by mesoscale activity *(11, 31)*, or lateral stirring by filaments *(32)*. In addition, multiple active vent fields have been (recently) identified along the Tonga arc and the Lau Basin *(16, 17, 33, 34)*, either at shallow depths (<500 m) or deeper (500-1000 m). Although all active shallow vents have not yet been discovered, with a density estimation of one active volcano center per 12 km of arc, fertilization processes such as those evidenced at Volcano #1 likely occur at many locations along the arc, further explaining the regional extent of the Chl*a* patch observed by satellite (Fig. 2A). We cannot exclude that the few emerged Tonga islands could provide additional nutrients, likely contributing to the observed bloom. However, a study conducted over the entire tropical Pacific reveals that these island mass effects are generally very localized (around the islands, with a Chl*a* patch area of 9-13 km^2) and are of moderate amplitude (+9% of Chl*a* increase relative to background waters) *(35)*. In contrast, the bloom in the region of the Tonga volcanic arc is unique in that it is much larger (360,000 km^2) and of greater amplitude (~100% Chl*a* increase) than around any other Pacific islands/archipelagos. This means that additional Fe sources of hydrothermal origin are necessary to sustain such a bloom. As an example, very weak Chl*a* is observed around the Cook Islands located at the same latitude as Tonga, receiving the same amount of rainfall and aerosol-Fe deposition annually, but not impacted by hydrothermal activity (Fig. S9), confirming that

nutrients of terrestrial origin are not sufficient to sustain blooms of large amplitude. Finally, some extremely rare events such as the massive eruption of the Hunga Tonga Hunga Ha'apai volcano in January 2022 could also cause short-term localized blooms, such as the one observed from satellite following the eruption *(36)*, that had no visible effect on the interannual trend of Chl*a*. Other authors suggest that the interpretation of the Chl*a* increase after the eruption was distorted by the presence of abundant volcanic particles suspended in the water column following the eruption *(37)*.

Looking more deeply into the 25-year monthly Chl*a* time series (Fig. 2B, S10), we find that, despite interannual variability, the bloom develops every year for at least 6 months in austral summer. This seasonal characteristic is probably linked to the thermal fitness of *Trichodesmium,* who are thought to only bloom at temperatures >25°C -reached in the WTSP between November and April (austral summer)-. This thermal constraint for *Trichodesmium* also probably explains why the bloom does not extend south of ~23°S, which marks the location of the 25°C isotherm. Further south, surface waters are also depleted in nitrate, and in the absence of diazotrophs, the new Fe supplied by hydrothermal vents along the arc cannot be taken up to produce new biomass. As models predict a sea surface temperature increase of 1.5°C by the end of the century in the Tonga arc region (*38*), it is possible that the thermal constraint for diazotrophs will be relieved and the bloom will spread further south in the future.

To properly account for the seasonal variability of export, we deployed a moored sediment trap at 1000 m for a full annual cycle in the fertilized patch (see SI). We show that POC export was 5 times higher in austral summer compared to winter (Fig. 4), resulting in a seasonally-integrated (6 summer months) POC export of 74 mmol C m^{-2}, i.e. 80% of the annual POC export flux. The low $\delta^{15}N$ signature of sinking PON during these summer months (~0-1‰) confirms that N_2 fixation supports most export production during that season. In austral winter, the higher sinking PON $\delta^{15}N$ values (2-8‰) suggest that other N sources (i.e., deep nitrate) fuel the low export production. For comparison, the annual POC flux measured here in the subtropical ocean is of the same order of magnitude as that measured in the Southern Ocean in naturally Fe-fertilized waters (*39, 40*). This suggests that Fe-fertilized regions of the oligotrophic ocean can act as net CO_2 sinks, provided sufficient phosphorus availability. The Fe-fertilized WTSP is a unique ecosystem allowing C sequestration supported by N_2 fixation due to substantial winter phosphate replenishment (not associated with nitrate supply due to decoupling of phosphacline and nitracline depths) (*25*) and to a turbulent diffusive flux of Fe and phosphate (19 mmol : mol^{-1}) meeting *Trichodesmium* requirements (*41*). Furthermore, *Trichodesmium* can reduce its P quotas under P stress (*42, 43*), and actively utilizes dissolved organic P (DOP) compounds in this region (*44*), likely enhanced by high Fe availability (*45*). Taken together, this suggests that P and Fe work in concert to trigger extensive diazotroph blooms and C sequestration by N_2-based new production in the WTSP.

Compared to shelf-driven natural Fe fertilizations occurring in HNLC (High Nutrient, Low Chlorophyll) waters of the Southern Ocean (SO), the TONGA bloom is generally more temporally and spatially extensive, despite its lower intensity (depth integrated Chl*a*) (Table 1) *(39, 46-48)*. The total DFe flux in this study (130 nmol Fe m^{-2} d^{-1}) was generally lower than that measured in Fe-enriched waters downstream of the Kerguelen plateau (KEOPS cruise in 2005, 222 nmol Fe m^{-2} d^{-1} *(49)*) and downstream of the Crozet plateau (CROZEX cruise in 2004, 550 nmol Fe m^{-2} d^{-1} *(39)*) (Table 1). However, unlike HNLC regions, surface waters of the WTSP are nitrate-depleted, and only N_2-fixing organisms can exploit this new Fe to build biomass and drive carbon export to the deep ocean, as long as sufficient phosphorus remains available. Based on the excess POC export and the excess of DFe supply at the time of the

cruise (Table 1), we calculated a C sequestration efficiency (defined as the ratio of the excess POC export to the amount of excess DFe supplied) of 13600 and 23000 mol C mol^{-1} Fe (at 170 and 270 m, respectively). Although comparisons between studies need to be considered with caution given the different methods used and timescales considered to estimate both excess Fe supply and POC export, this sequestration efficiency is higher than those from artificial mesoscale Fe-addition experiments (e.g. 4300 mol mol^{-1} for SOFeX *(50)*; 1200 mol mol^{-1} for SERIES *(51)*), and in the range of values measured in naturally-fertilized HNLC regions (8600 mol mol^{-1} for CROZEX *(39)* to 154,000 mol mol^{-1} during KEOPS *(49)*). This confirms that natural Fe fertilizations are more efficient for carbon sequestration than purposeful Fe additions. In addition, comparing such estimates from various natural oceanic settings, Le Moigne et al. *(52)* suggested that the apparent variability in C sequestration efficiency may be related to the timescale of Fe delivery (slow delivery being more efficient). Therefore, attention must be paid in future studies to the timescale of delivery of this newly-recognized mode of Fe supply through shallow hydrothermalism, including in temperate and polar ecosystems, where this efficiency could be even more important due to higher macronutrient availability.

Our conceptual view of the ocean Fe cycle has greatly evolved over the past 10 years, highlighting the importance of hydrothermal activity on the Fe cycle *(53)*. While model simulations suggest that hydrothermal inputs associated with mid-ocean ridges (>2000 m) contribute 23% of the Fe found in the global ocean water column, that Fe only directly supports 3% of carbon export at 100 m *(54)*. This is mostly because a large part of that Fe remains in the deep ocean over long time scales *(53)* and needs to be entrained in surface waters before potentially impacting photosynthetic communities *(46, 48)*. Fe from intermediate depth (~1000 m) vents may also be transported long distances and with the condition that these waters upwell, influence marine ecosystems located thousands of km far from the site of discharge *(55)*. However, hydrothermal venting also occurs at shallower depths (<500 m) in island arc systems such as the Tonga arc. Even if scavenging and precipitation removes part of this newly-emitted Fe from the dissolved pool *(23)*, such shallow sources can supply Fe rapidly to overlying surface photosynthetic communities compared to Fe emitted deeper *(23, 55)*. In the oligotrophic ocean, the implications of such shallow hydrothermal Fe fertilization are highly significant as they directly fuel surface diazotrophs and export of organic matter to the deep ocean, representing regional hotspot sinks of atmospheric CO_2. We demonstrate here that shallow hydrothermal sources also represent a triggering factor on diazotroph blooms in regions where the atmospheric supply of DFe is virtually absent. Such forcing is of the utmost importance to study as climate models predict an expansion of the oligotrophic gyres (40% of our oceans) *(56)* where diazotrophs will likely thrive. Furthermore, in a warmer, more stratified ocean, such shallow Fe sources are likely to deliver Fe to surface communities more readily than deep sources *(55)*. Beyond the oligotrophic oceans, shallow hydrothermal fertilizations are likely to be common in the global ocean, due to the high number of shallow hydrothermal vents associated with island arc systems and submarine volcanic calderas (*57*) whose exact number/locations are still yet to be discovered *(14)*. Such systems are also present at higher latitudes, notably in the HNLC waters in the subarctic Pacific and the SO *(57)*. Therefore, a comprehensive evaluation of their impact in these severely Fe-limited systems where surface mixed layers reach the intermediate or even the deep ocean water masses is clearly needed. Finally, the extent to which such hydrothermal-driven biological carbon pump enhancement may have changed atmospheric CO_2 in the past remains unclear. Future studies would be relevant as the hydrothermal flux of Fe has been relatively constant over millennial timescales *(58)*.

References and Notes

1. C. M. Moore *et al.*, Processes and patterns of oceanic nutrient limitation. *Nature Geoscience* **6**, 701–710 (2013).
2. N. Gruber, in *Nitrogen in the marine environment*. (2008), pp. 1-50.
3. S. Bonnet *et al.*, Diazotrophs are overlooked contributors to carbon and nitrogen export to the deep ocean. *The ISME journal* **17**, 47-58 (2022).
4. D. M. Karl, M. J. Church, J. E. Dore, R. Letelier, C. Mahaffey, Predictable and efficient carbon sequestration in the North Pacific Ocean supported by symbiotic nitrogen fixation. *Proceedings of the National Academy of Sciences* **109**, 1842–1849 (2012).
5. A. Subramaniam *et al.*, Amazon River enhances diazotrophy and carbon sequestration in the tropical North Atlantic Ocean. *Proceedings of the National Academy of Sciences* **105**, 10460–10465 (2008).
6. J. P. Zehr, D. G. Capone, Changing perspectives in marine nitrogen fixation. *Science* **368**, (2020).
7. C. Lory *et al.*, Assessing the contribution of diazotrophs to microbial Fe uptake using a group specific approach in the Western Tropical South Pacific Ocean. *ISME Communications* **2**, 1-11 (2022).
8. J. A. Sohm, E. A. Webb, D. G. Capone, Emerging patterns of marine nitrogen fixation. *Nature Reviews Microbiology* **9**, 499-508 (2011).
9. S. Bonnet, M. Caffin, H. Berthelot, T. Moutin, Hot spot of N2 fixation in the western tropical South Pacific pleads for a spatial decoupling between N2 fixation and denitrification. *Proceedings of the National Academy of Sciences* **114**, E2800-E2801 (2017).
10. C. Schlosser *et al.*, Seasonal ITCZ migration dynamically controls the location of the (sub)tropical Atlantic biogeochemical divide. *Proceedings of the National Academy of Sciences of the United States of America* **111**, 1438-1442 (2014).
11. C. Guieu *et al.*, Iron from a submarine source impacts the productive layer of the Western Tropical South Pacific (WTSP). *Scientific Reports* **8**, 9075 (2018).
12. L. Bopp *et al.*, Diazotrophy as a key driver of the response of marine net primary productivity to climate change. *Biogeosciences* **19**, 4267-4285 (2022).
13. C. E. J. de Ronde *et al.*, in *Volcanic, Geothermal, and Ore-Forming Fluids: Rulers and Witnesses of Processes within the Earth*. (Society of Economic Geologists, 2005), vol. 10, pp. 0.
14. C. R. German *et al.*, Hydrothermal impacts on trace element and isotope ocean biogeochemistry. *Phil. Trans. R. Soc. A* **374**, 20160035 (2016).
15. J. E. Lupton, D. G. Pyle, W. J. Jenkins, R. Greene, L. Evans, Evidence for an extensive hydrothermal plume in the Tonga-Fiji region of the South Pacific. *Geochem Geophy Geosy* **5**, (2004).
16. P. Stoffers *et al.*, Submarine volcanoes and high-temperature hydrothermal venting on the Tonga arc, southwest Pacific. *Geology* **34**, 453-456 (2006).
17. G. Massoth *et al.*, Multiple hydrothermal sources along the south Tonga arc and Valu Fa Ridge. *Geochemistry, Geophysics, Geosystems* **8**, (2007).
18. C. Guieu, S. Bonnet, TONGA GEOTRACES GPpr14 ocean expedition, https://doi.org/10.17600/18000884. (2019).
19. C. Boulart *et al.*, Active hydrothermal vents in the Woodlark Basin may act as dispersing centres for hydrothermal fauna. *Commun Earth Environ* **3**, (2022).
20. W. W. Chadwick *et al.*, Imaging of CO2 bubble plumes above an erupting submarine volcano, NW Rota-1, Mariana Arc. *Geochem Geophy Geosy* **15**, 4325-4342 (2014).
21. N. Feuillet *et al.*, Birth of a large volcanic edifice offshore Mayotte via lithosphere-scale dyke intrusion. *Nature Geoscience* **14**, 787-+ (2021).

22. J. A. Resing *et al.*, Basin-scale transport of hydrothermal dissolved metals across the South Pacific Ocean. *Nature* **523**, 200-203 (2015).
23. C. Tilliette *et al.*, Dissolved Iron Patterns Impacted by Shallow Hydrothermal Sources Along a Transect Through the Tonga-Kermadec Arc. *Global Biogeochemical Cycles* **36**, e2022GB007363 (2022).
24. J. Lavelle, I. Lozovatsky, D. Smith IV, Tidally induced turbulent mixing at Irving Seamount—modeling and measurements. *Geophysical research letters* **31**, (2004).
25. T. Moutin *et al.*, Nutrient availability and the ultimate control of the biological carbon pump in the western tropical South Pacific Ocean. *Biogeosciences* **15**, 2961-2989 (2018).
26. Y.-W. Luo *et al.*, Database of diazotrophs in global ocean: abundance, biomass and nitrogen fixation rates. *Earth System Science Data* **4**, 47-73 (2012).
27. A. Filella *et al.*, Contrasting Roles of DOP as a Source of Phosphorus and Energy for Marine Diazotrophs. *Frontiers in Marine Science* **9**, (2022).
28. F. Van Wambeke *et al.*, Dynamics and controls of heterotrophic prokaryotic production in the western tropical South Pacific Ocean: links with diazotrophic and photosynthetic activity. *Biogeosciences* **15**, 2669-2689 (2018).
29. M. Benavides *et al.*, Sinking Trichodesmium fixes nitrogen in the dark ocean. *The ISME journal* **16**, 2398-2405 (2022).
30. A. N. Knapp *et al.*, Distribution and rates of nitrogen fixation in the western tropical South Pacific Ocean constrained by nitrogen isotope budgets. *Biogeosciences* **15**, 2619-2628 (2018).
31. L. Rousselet *et al.*, Large- to submesoscale surface circulation and its implications on biogeochemical/biological horizontal distributions during the OUTPACE cruise (southwest Pacific). *Biogeosciences* **15**, 2411-2431 (2018).
32. A. de Verneil, L. Rousselet, A. M. Doglioli, A. A. Petrenko, T. Moutin, The fate of a southwest Pacific bloom: gauging the impact of submesoscale vs. mesoscale circulation on biological gradients in the subtropics. *Biogeosciences* **14**, 3471-3486 (2017).
33. S. E. Beaulieu, E. T. Baker, C. R. German, A. Maffei, An authoritative global database for active submarine hydrothermal vent fields. *Geochem Geophy Geosy* **14**, 4892-4905 (2013).
34. C. R. German *et al.*, Hydrothermal impacts on trace element and isotope ocean biogeochemistry. *Philosophical Transactions of the Royal Society A: Mathematical, Physical and Engineering Sciences* **374**, (2016).
35. M. Messie, A. Petrenko, A. M. Doglioli, E. Martinez, S. Alvain, Basin-scale biogeochemical and ecological impacts of islands in the tropical Pacific Ocean. *Nature Geoscience* **15**, 469-+ (2022).
36. B. Barone, R. M. Letelier, K. H. Rubin, D. M. Karl, Satellite Detection of a Massive Phytoplankton Bloom Following the 2022 Submarine Eruption of the Hunga Tonga-Hunga Ha‘apai Volcano. *Geophysical Research Letters* **49**, e2022GL099293 (2022).
37. A. Whiteside *et al.*, Impact of ashes from the 2022 Tonga volcanic eruption on satellite ocean color signatures. *Frontiers in Marine Science* **9**, (2023).
38. L. Dhage, M. J. Widlansky, Assessment of 21st Century Changing Sea Surface Temperature, Rainfall, and Sea Surface Height Patterns in the Tropical Pacific Islands Using CMIP6 Greenhouse Warming Projections. *Earths Future* **10**, (2022).
39. R. T. Pollard *et al.*, Southern Ocean deep-water carbon export enhanced by natural iron fertilization. *Nature* **457**, 577-580 (2009).
40. M. Rembauville, I. Salter, N. Leblond, A. Gueneugues, S. Blain, Export fluxes in a naturally iron-fertilized area of the Southern Ocean - Part 1: Seasonal dynamics of

particulate organic carbon export from a moored sediment trap. *Biogeosciences* **12**, 3153-3170 (2015).
41. J. Nuester, S. Vogt, M. Newville, A. B. Kustka, B. S. Twining, The unique biogeochemical signature of the marine diazotroph trichodesmium. *Frontiers in microbiology* **3**, 150 (2012).
42. D. M. Karl, R. Letelier, D. V. Hebel, D. F. Bird, C. D. Winn, *Trichodesmium blooms and new nitrogen in the North Pacific Gyre*. C. D. G. R. J. G. Carpenter E.J., Ed., Marine pelagic cyanobacteria:Trichodesmiurn and other diazotrophs. (Kluwer Academic Publishers, Dordrecht, 1992), pp. 219-237.
43. A. E. White, Y. H. Spitz, D. M. Karl, R. M. Letelier, Flexible elemental stoichiometry in Trichodesmium spp. and its ecological implications. *Limnology and Oceanography* **51**, 1777-1790 (2006).
44. Z. Liang, R. T. Letscher, A. N. Knapp, Dissolved organic phosphorus concentrations in the surface ocean controlled by both phosphate and iron stress. *Nature Geoscience* **15**, 651-+ (2022).
45. T. J. Browning *et al.*, Iron limitation of microbial phosphorus acquisition in the tropical North Atlantic. *Nature Communications* **8**, (2017).
46. M. Ardyna *et al.*, Hydrothermal vents trigger massive phytoplankton blooms in the Southern Ocean. *Nat Commun* **10**, 2451 (2019).
47. S. Blain, S. Bonnet, C. Guieu, Dissolved iron distribution in the tropical and sub tropical South Eastern Pacific. *Biogeosciences* **5**, 269–280 (2008).
48. C. M. S. Schine *et al.*, Massive Southern Ocean phytoplankton bloom fed by iron of possible hydrothermal origin. *Nat Commun* **12**, 1211 (2021).
49. S. Blain *et al.*, Effect of natural iron fertilization on carbon sequestration in the Southern Ocean. *Nature* **446**, 1070-1074 (2007).
50. K. O. Buesseler, J. E. Andrews, S. M. Pike, M. A. Charette, The effect of iron fertilization on carbon sequestration in the Southern ocean. *Science* **304**, 414-417 (2004).
51. P. W. Boyd *et al.*, The decline and fate of an iron-induced subarctic phytoplankton bloom. *Nature* **428**, 549-553 (2004).
52. F. A. C. Le Moigne *et al.*, Sequestration efficiency in the iron-limited North Atlantic: Implications for iron supply mode to fertilized blooms. *Geophysical Research Letters* **41**, 4619-4627 (2014).
53. A. Tagliabue *et al.*, The integral role of iron in ocean biogeochemistry. *Nature* **543**, 51-59 (2017).
54. A. Tagliabue, O. Aumont, L. Bopp, The impact of different external sources of iron on the global carbon cycle. *Geophysical Research Letters* **41**, 920-926 (2014).
55. W. Jenkins *et al.*, An intermediate-depth source of hydrothermal 3He and dissolved iron in the North Pacific. *Earth and Planetary Science Letters* **539**, 116223 (2020).
56. J. J. Polovina, E. A. Howell, M. Abecassis, Ocean's least productive waters are expanding. *Geophysical Research Letters* **35**, (2008).
57. J. A. Hawkes, D. P. Connelly, M. J. A. Rijkenberg, E. P. Achterberg, The importance of shallow hydrothermal island arc systems in ocean biogeochemistry. *Journal of Geophysical Research*, (2014).
58. N.-C. Chu *et al.*, Evidence for hydrothermal venting in Fe isotope compositions of the deep Pacific Ocean through time. *Earth and Planetary Science Letters* **245**, 202-217 (2006).

Acknowledgments: The dataset presented here resulted from the efforts of many individuals both onboard and on land who contributed to the success of the expedition. We thank the captain

and the crew of the R/V *L'Atalante* (TGIR Flotte, operated by IFREMER), in particular S. Laville Saint-Martin and J. Le Doare for their help during the multibeam survey, as well as the Technical Division INSU for the provision of the equipment. We thank the captain and the crew of the R/V *Alis* (TGIR Flotte, operated by IFREMER), for the safe recovery of the fixed mooring in particularly difficult weather conditions. We thank Céline Dimier and the SAPIGH platform of the Institut de la Mer de Villefranche (IMEV) for sampling on board and performing the pigment analyses. Finally, we thank Mr Lucas Jr for the English editing. Finally we are very grateful and thank JP Gattuso, S. Blain, A. Tagliabue and L. Guidi for their advice on the manuscript.

Funding:
Agence Nationale de Recherche grant ANR-18-CE01-0016 (SB, CG)
A-Midex grant TONGA (SB, CG)
Institut National des Sciences de l'Univers Les Enveloppes Fluides et l'Environnement grant TONGA (SB, CG)
TGIR Flotte océanographique française TONGA cruise (CG, SB)
MEMESTRA Grant (CB)
US NSF-OCE 1829797 (ANK)

Author contributions:
Conceptualization: SB, CG
Methodology: SB, CG, CB, FG
Investigation: SB, CG, VT, CB, FG, MB, DGS, JMG, OG, JH, CL, EP, GS, CT
Data curation: SB, CG, VT, CB, PBA, CS, FG, MB, ANK, YC, DGS, HJF, JH, NL, SN, ALR, GS, CS
Visualization: SB, CG, CB, FG, PBA, ANK, HJF
Writing – original draft: SB, CG
Writing – review & editing: All

Competing interests: Authors declare that they have no competing interests.
Data and materials availability: All data are available in the main text or the supplementary materials. The delta ^{15}N data are deposited to the BCO-DMO database https://www.bco-dmo.org/dataset/869963. The biogeochemical data are deposited on the INSU-LEFE-CYBER database http://www.obs-vlfr.fr/proof/php/TONGA/tonga_log_basicfiles.php and the acoustic data on the SEANOE database https://campagnes.flotteoceanographique.fr/campagnes/18000884/

Supplementary Materials
Materials and Methods
References (1-32)
Figs. S1 to S10
Tables S1 to S5

Figure legends.

Fig. 1. Acoustic, optical and chemical anomalies measured above Volcano #1. (A) Location map showing the Tonga volcanic arc system and Volcano #1 (V1, red triangle, -21.154; 175.744). (B) Bathymetry of Volcano #1 performed during TONGA, and position of the fluid/gas active sites detected by the multibeam echo sounder (EM710, 70-110 kHz) during the survey. The white circle represents the specific site studied here ('Panamax site'), from which the data are shown in panels C, D, E, F. (C) Multibeam echo sounder image (EM710, 70-110 kHz) showing hydrothermal gas and fluid emissions from the seafloor rising up to ~10 m below the sea surface. (D) Time series (11h) of acoustic signal detected by the sounder EK60 (38kHz) showing gas/fluid seafloor emissions at a fixed position (visualization threshold -75dB). (E) Vertical CTD profiles of temperature, pH, turbidity, and Eh in the main acoustic signal. (F) Vertical profiles of methane (CH_4, nM), dissolved Mn (nM), and dissolved Fe (nM) concentrations above Volcano #1.

Fig. 2. Chlorophyll patch in the vicinity of Tonga and associated biogeochemical and biological parameters. (A) Surface [Chl*a*] MODIS composite averaged over the time period corresponding to the TONGA cruise (1 November-6 December 2019) at a resolution of 4 km and zoom of the bloom region (~360 000 km^2). The bloom is delineated by the isoline 0.9 µg $liter^{-1}$ (corresponding to twice the average background [Chl*a*] concentration outside the bloom. (B) Monthly climatology of [Chl*a*] from a 25 years-time series (GLOBCOLOR product) at 2 sites along 20°S; the red line corresponds to the region of the Tonga bloom represented with the red dot on panel (A), and the blue line corresponds to the location of the reference site in the South Pacific Gyre, represented as a blue dot on panel (A). Horizontal and vertical distributions of (C) Total Chl*a* concentrations (µg L^{-1}), (D) Particulate organic nitrogen concentrations (µmol L^{-1}), (E) N_2 fixation rates (nmol N L^{-1} d^{-1}), (F) *Trichodesmium* abundances (Log nifH gene copies L^{-1}), (G) Dissolved Fe concentrations (nmol $liter^{-1}$). Y axis: depth (m), X axis: longitude; grey dots correspond to sampling depths at the various stations.

Fig. 3. Experimental evidence of the impact of hydrothermally-enriched water additions on diazotroph communities. Temporal evolution of (A) N_2 fixation rates (nmol N L^{-1} d^{-1}), (B) *Trichodesmium* abundances (*nifH* gene copies L^{-1}) along the 196h of the experiment in the control treatment (no fluid addition), and in the reactors amended with 1.8%, 5.5%, and 14.5% of 'plume water' collected at the 'Panamax site' of Volcano #1 (~200 m depth). Error bars correspond to standard deviations on triplicate analyses.

Fig. 4. Seasonal variability of export at 1000 m in the Fe-fertilized patch over one year (fixed mooring deployed at -20.702; -177.866 from Nov. 2019-Nov 2020; see SI)). Blue line: particulate organic carbon (POC) export fluxes (mmol C m^{-2} d^{-1}). Red line: δ15N (per mil) signature of exported PON.

Table 1. Carbon and Fe budgets in the naturally-fertilized region of the Tonga volcanic arc and the distal reference site, and comparisons with natural fertilizations in HNLC regions.

	TONGA		CROZEX (2,5)	KEOPS (2,3)
	+Fe (Volcano #1)	-Fe (Gyre)		
Bloom area (km^2)	360000	No bloom	90000	45000
Bloom duration (d)	180	-	58	75-105
Integrated Chla over the euphotic zone (mg Chl*a* m^{-2})	39	-	98.1	72-318
Vertical diffusivity (Kz, m^2 s^{-1})	$3.7 \pm 1.9 \times 10^{-5}$	$5.2 \pm 9.6 \times 10^{-6}$		
Vertical DFe gradient (mol m^{-4})	$3.1 \pm 4.7 \times 10^{-8}$	$7.8 \pm 3.1 \times 10^{-11}$		
Vertical DFe diffusive flux (mmol Fe m^{-2} d^{-1})	$1.1 \pm 1.7 \times 10^{-4}$	$3.5 \pm 3.1 \times 10^{-8}$	6.0×10^{-5}	3.1×10^{-5}
Atmospheric DFe supply (mmol Fe m^{-2} d^{-1}) (1)	2.0×10^{-5}	2.5×10^{-5}	1.0×10^{-4}	1.7×10^{-6}
Horizontal DFe supply (mmol Fe m^{-2} d^{-1})	0 (4)	0 (4)	3.9×10^{-4}	1.9×10^{-4}
Total DFe supply (mmol Fe m^{-2} d^{-1})	1.3×10^{-4}	2.5×10^{-5}	5.5×10^{-4}	2.2×10^{-4}
Total annual DFe supply (mmol Fe m^{-2})	4.7×10^{-2}	0.9×10^{-2}	20.0×10^{-2}	8.1×10^{-2}
POC export 170 m (mmol C m^{-2} d^{-1})	3.2	1.7		
POC export 270 m (mmol C m^{-2} d^{-1})	3.9	1.4		
"Excess" C sequestration efficiency Ceffx 170 m (mol C mol^{-1} Fe)	13600	-	8640	154000
"Excess" C sequestration efficiency Ceffx 270 m (mol C mol^{-1} Fe)	23000	-		

(1) Guieu et al., (2018)
(2) Morris & Charrette, (2013)
(3) Blain et al., (2007) updated by Chever et al., (2010)
(4) The main flux is from below, lateral advection is likely negligible
(5) Pollard et al., (2009)

Science
AAAS

Supplementary Materials for

Natural iron fertilization by shallow hydrothermal sources fuels diazotroph blooms in the Ocean

Authors: Sophie Bonnet[1], Cécile Guieu[2], Vincent Taillandier[2], Cédric Boulart[3], Pascale Bouruet-Aubertot[4], Frédéric Gazeau[2], Carla Scalabrin[5], Matthieu Bressac[2], Angela N. Knapp[6], Yannis Cuypers[4], David González-Santana[7,8], Heather J. Forrer[6], Jean-Michel Grisoni[9], Olivier Grosso[1], Jérémie Habasque[7], Mercedes Jardin-Camps[1], Nathalie Leblond[2], Frédéric Le Moigne[1,7], Anne Lebourges-Dhaussy[7], Caroline Lory[1], Sandra Nunige[1], Elvira Pulido-Villena[1], Andrea L. Rizzo[10,11], Géraldine Sarthou[7], Chloé Tilliette[2]

***Correspondence to:** sophie.bonnet@mio.osupytheas.fr, cecile.guieu@imev-mer.fr

This PDF file includes
Materials and Methods
Figs. S1 to S10
Tables S1 to S5
References (1-32)

Materials and Methods

Fieldwork design

Data were acquired during the GEOTRACES-endorsed TONGA (Shallow hydroThermal sOurces of trace elemeNts: potential impacts on biological productivity and the bioloGicAl carbon pump) expedition (October 30-December 6, 2019, https://doi.org/10.17600/18000884) on board the R/V L'Atalante). The general strategy consisted in: i) a 3000 km transect crossing the Tonga volcanic arc at 20-21°S, sampling 12 stations located both sides of the arc, namely Melanesian archipelago waters and South Pacific Gyre waters, ii) an intensive 5-days survey on the Tonga volcanic arc to locate a 'case study' shallow (~200 m) volcano associated with hydrothermal activity (Volcano #1), to investigate the direct potential effect of hydrothermal fluids on biological stocks and fluxes.

Acoustic plume detection

Shipborne single and multibeam echosounder surveys were carried out over the targeted volcano to detect putative gas and/or fluid emissions (*1*) . Surveys were performed at <7 knots using the hull-mounted EM-122 and EM-710 echosounders of R/V L'Atalante, operating at a frequency of 12 kHz (for depths >1000m), and 70 to 100 kHz (for lower depths), respectively. Our strategy allowed us to establish a high-resolution (10 m) bathymetric mapping of the targeted area; simultaneously, acoustic anomalies directly identified on the screen during the survey and corresponding to putative fluid emissions were reported in order to get all the coordinates where anomalies were detected. Acoustic anomalies were considered as attributable to hydrothermal emissions if they were connected to the seafloor and reproducible over time. Multibeam data were processed during the cruise and post-processed at land using SonarScope (*2*) and GLOBE (*3*) softwares. After having located the site showing the highest anomaly (Fig. 1A), the second step consisted in deploying a conductivity–temperature–pressure (CTD) rosette fitted with Niskin bottles and additional physical and chemical sensors (see next paragraph) to confirm the presence of chemical and physical/optical anomalies related to hydrothermal plumes in the water column. At that specific site (the 'Panamax site'), the R/V remained 11 hours above and within a short distance from that source, also allowing to perform a time-series of acoustic anomalies using a calibrated *(4)* Simrad EK60 echosounder operating at 38 kHz with an average ping interval of 5 s (Fig. 1D). The pulse length was set at 1024 µs and transmit powers was 2000 W.

Optical and chemical plume detection

The chemical plume survey was carried out using a 12-Niskin CTD-rosette frame fitted with two turbidimeters (Seapoint Turbidity Meters), a pH sensor and a Eh sensor (both from AMT GmBH), interfaced to a SBE911+ (Seabird Electronics). The CTD-rosette was deployed either as vertical casts or as towed casts ('tow-yo casts'). During vertical casts, the CTD-rosette was lowered in the water column at 1 m per second or less to the deepest point. Niskin bottles were fired during up-casts at different levels in the water column, whenever an anomaly of T, S, turbidity or Eh appeared on the real-time data display. The tow-yo casts consisted in lowering and raising the CTD-rosette between a constant set depth and a few meters above the seafloor while the ship moved along a transect at a maximum speed of 0.4 knot.

Water samples for dissolved gas analysis (methane (CH_4), Helium (He)) were drawn from the Niskin bottles and processed straight after the CTD-rosette was brought back on board. 20 mL-headspace glass vials were flushed with the water from the Niskin bottles, filled until overflow, poisoned, and crimp-sealed to avoid any air contamination. Water samples for Helium isotopes analysis were transferred from the Niskin into copper tubes that were clamped on both ends

paying attention to avoid the entrapment of any air bubbles. This storage is typical of water sampling aimed at measurements of dissolved noble gases *(5)*.

Dissolved CH_4 concentrations were determined on board using the headspace extraction technique followed by GC-FID. Duplicates were analyzed back on shore on a Shimadzu GC-BID coupled to a HS-20 to confirm the on-board measurements. He isotopes were analyzed in the noble gas laboratory of INGV-Palermo (Italy). Copper tubes were connected to a stainless steel extraction line maintained under high-vacuum and equipped with a pyrex bulbe and a manometer. The extraction of helium and neon dissolved in the water was carried out by following standard protocols *(5, 6)*. The following He (^{3}He, ^{4}He) and ^{20}Ne isotopic measurements followed the analytical method reported in Rizzo et al., (2016) *(7)*. The concentrations of He and Ne are reported in cc/l STP, while the ^{3}He/^{4}He ratio is expressed as R/Ra (being Ra the He isotopic ratio of air and equal to 1.39×10^{-6}).

Dissolved Fe and Mn concentrations

Seawater samples were collected above Volcano #1 and at 12 stations along the transect according to the GEOTRACES guidelines (www.geotraces.org/images/Cookbook.pdf), using a Trace Metal Clean Rosette (TMR, General Oceanics Inc. Model 1018 Intelligent Rosette) attached to a 6 mm Kevlar line and fitted with 24 Go-Flo bottles. Immediately after collection, the entire rosette was transferred into a clean container for sampling. The cleaning protocols for sampling bottles and equipment also followed the GEOTRACES Cookbook. Samples for the determination of total dissolved iron (DFe) and manganese (DMn) concentrations were filtered on-line through 0.45 µm using a polyethersulfone filter (Supor®). All samples were acidified within 24h of collection with ultrapure hydrochloric acid (HCl, Merck, 0.2%, final pH 1.7). Dissolved iron (DFe) were analyzed by Flow Injection Analysis with chemiluminescence detection *(8)*. Dissolved Mn was analyzed using a preconcentration system SeaFAST coupled to a high resolution magnetic sector field inductively coupled mass spectrometer (HR-ICP-MS, Element XR) method following Tonnard et al. (2020) *(9)*.

Vertical eddy diffusivity (Kz) measurements and DFe vertical fluxes estimates

Microstructure measurements were performed using a vertical microstructure profiler 'VMP250' (Rockland Scientific). This tethered profiler was equipped with microstructure sensors, two shear sensors, and two temperature sensors, as well as with Sea-Bird temperature and conductivity sensors.

Four VMP profiles were performed above Volcano #1. The dissipation rate of turbulent kinetic energy (epsilon) was inferred from centimeter-scale shear measurements as described in Bouruet-Aubertot et al, (2018) *(10)*. The vertical eddy diffusivity (Kz) was then inferred from the kinetic energy dissipation rate using the Osborn (1980) *(11)* relationship:

$$Kz = \text{Gamma} \times \text{epsilon}\ N^{-2}$$

where Gamma is a mixing efficiency defined as the ratio between the buoyancy flux and the dissipation rate, and N the buoyancy frequency. The kinetic energy dissipation rate is computed over 1m bin, and a 8-m moving average is then applied, while the buoyancy frequency square is inferred from the VMP Sea-Bird temperature and conductivity sensors, with a 8-m moving average applied on this signal after preliminary processing to eliminate spurious spikes on the salinity signal. Gamma is set to 0.2 provided that turbulence intensity values fall within the intermediate regime where the Osborn relationship applies (see further details in Bouruet-Aubertot et al, 2018) *(10)*.

DFe vertical supply at station Volcano #1 was estimated based on turbulent diffusive flux:

$$F = -Kz \times dcFe/dz$$

where dcFe/dz is the vertical gradient of DFe concentration, cFe. As the DFe concentration profile displays variations, the DFe turbulent diffusive flux is either upward or downward with strong variations in absolute value as a result of vertical eddy diffusivity variations within 1 or 2 orders of magnitude (Fig. S2). Mean values of DFe input as well as their standard deviations were computed over the mixed layer (within [40m-60m]), where most of the biological biomass needing Fe was concentrated.

The instrument was lost after Volcano #1, and in the absence of VMP measurements at the reference site, the vertical eddy diffusivity, Kz, was inferred from CTD measurements. This Kz estimate was based on the Thorpe scale method *(12, 13)* when density overturns are detected by CTD with a given threshold for noise taken here to 3x10-4 kg.m-3. Kz (term 1) is proportional to the mean square of vertical displacements within the overturn. In addition, a 'background' value for Kz (term 2) was inferred from the strain computed over vertical segments of 256 m extension, following Kunze et al (2006) *(14)*. The intermediate Kz value equals the sum (1) + (2).

The method was first validated at the Volcano#1 station, where CTD data were collected just after the VMP profiles (TMC12). The 'background' value for Kz (term 2) was computed over the length of the CTD profile, 194 m, the proportionality constant for Kz term 1 was adjusted with VMP measurements and a 20 m moving average was applied to Kz term1 (see Fig. S3).

The same procedure based on CTD measurements was applied at the reference station in the gyre for the computation of Kz as described above. An optimal interpolation was applied to DFe values in the first 1000 m in order to eliminate unrealistic variations, of the order of 10^{-7} mol m^{-3} prior to the flux computation (Fig. S4). Vertical eddy diffusivity, vertical gradient of DFe concentration and turbulent diffusive flux within the base of the mixed layer and the ferricline are displayed in Table 1.

SVP drifters trajectories

Three clusters, each composed of 5 SVP drifters have been deployed at the Volcano #1 station and at two additional stations along the Tonga arc (Station 12: -20.702; -177.866 and Station 10: -19.421; -174.901). Drifters are composed of a 35 cm sphere surface floats and a holey sock drogues centered at 15 m depth. GPS-based tracking is sent by Iridium communication. The obtained trajectories have a temporal resolution of some hours up to one day. Raw data are presented in Fig. S8. Patterns of dispersion appear contrasted for the three sites: in the western edge of the Lau Basin (left panel), trajectories indicate westward advection during the first three months. On the other hand, in the eastern site of the Lau Basin (middle and right panels), advective components are reduced and relative dispersion is the predominant pattern. Although qualitative, this description suggests larger horizontal eddy diffusivity along the Tonga arc compared to the Lau Basin.

The Tonga arc might be subject to intense dynamical features that occur in the surface layer, associated to the interaction of a steep topographic sill and basin-scale current system in the sub-tropical band. Drifter trajectories provide a bulk representation of a complex underlying dynamics, which develops at smaller scales with significant vertical component (upwelling).

In consequence for the iron budgets above the Volcano site, transports in the surface layer would be predominantly due to horizontal mixing rather than advection.

Ocean Color

Chlorophyll concentrations (mg m^{-3}) were provided by the global Ocean Color satellite observations from the Copernicus-GlobColour database. Two products have been used for this study, both processed from multi-satellite sensors with a spatial resolution of 4 km, and reprocessed using a consolidated input dataset and a unique algorithm: the composite image contemporary to the cruise (Fig. 1A) was extracted from the daily "Level 3" product (https://doi.org/10.48670/moi-00098). All seasonal cycles (Fig. 1B, Fig. S9 and Fig. S10) were extracted from the "Level 4" product ("cloud free") (https://doi.org/10.48670/moi-00100), in which a temporal averaging method was applied to fill-in missing data values. Each seasonal cycle was computed as follows: 25-year time series (from September 1997 to December 2022) were extracted at five locations along the 20°S parallel. For each month of the year, a mean value and standard deviation were computed.

Nitrate, phosphate concentrations

Nitrate, phosphate concentrations were measured at 12 stations along the west to east transect. Seawater samples were collected at 6 to 9 depths between 0 and 200 m using Niskin® bottles attached to the CTD-rosette. Samples for the quantification of nitrate and phosphate concentrations were collected in acid-washed polyethylene bottles after online filtration (0.2 µm, Sartorius Sartobran P capsule), frozen at -20°C until analysis. Concentrations were determined using standard colorimetric techniques *(15)* on a Bran Luebbe AA3 autoanalyzer. Quantification limits for the procedures were 0.05 µmol $liter^{-1}$ for nitrate and 0.02 µmol $liter^{-1}$ for phosphate. The same procedures were used for samples collected in the minicosms (see below).

Particulate organic nitrogen concentrations

Particulate organic nitrogen concentrations were measured at 9 stations along the west to east transect. Seawater samples were collected in 4.4 polycarbonate bottles at 6 depths between 0 and 150 m using Go-Flo bottles mounted on the trace metal clean rosette. The entire bottle was filtered onto pre-combusted (450°C, 4h) 25 mm diameter glass fiber filters (GF/F, Whatman, 0.7 µm nominal pore size). Filters were subsequently dried at 60°C for 24 h before analysis of $^{15}N=^{14}N$ ratios and particulate N (PN) using an elemental analyzer coupled to a mass spectrometer (EA-IRMS, Integra 2, SerCon Ltd) as described in Bonnet et al. (2018) *(16)*.

N_2 fixation rates

N_2 fixation rates were measured under trace metal clean conditions at 9 stations along the west to east transect. Seawater samples were collected in triplicate 2.3 polycarbonate bottles at 6 depths between 0 and 150 m using Go-Flo bottles mounted on the trace metal clean rosette. Rates were measured using the $^{15}N_2$ assimilation technique; the $^{15}N_2$ bubble technique was intentionally chosen to avoid any potential overestimation due to trace metal and dissolved organic matter contaminations often associated with the preparation of the $^{15}N_2$-enriched seawater *(17)*, as both have been found to control N_2 fixation or *nifH* gene expression in this region *(18, 19)*. Bottles were amended with 2 mL of 98.9 at.% $^{15}N_2$ (Cambridge isotopes), and incubated in on-deck incubators connected to surface circulating seawater and shaded at the specified irradiances using blue screening. Incubations were stopped by filtering the entire incubation bottle onto pre-combusted (450°C, 4h) 25 mm diameter glass fiber filters (GF/F, Whatman, 0.7 µm nominal pore size). Filters were subsequently dried at 60°C for 24 h before analysis of $^{15}N=^{14}N$ ratios and particulate N (PN) determinations using an elemental analyzer coupled to a mass spectrometer (EA-IRMS, Integra 2, SerCon Ltd) as described in Bonnet et al. (2018) *(16)*. The $^{15}N/^{14}N$ ratio of the N_2 pool available for N_2 fixation (the term AN_2 used in Montoya et al., 1996) (*20*) was measured in all incubation bottles by membrane inlet mass

spectrometry (MIMS) (*21*) to ensure accurate rate calculations as fully described in Bonnet et al., (2018) *(16)*. The same procedures were used for samples collected in the minicosms (see below).

Trichodesmium spp. abundances

Trichodesmium spp. abundances were estimated using quantitative PCR (qPCR) targeting the *nifH* gene, which encodes a subunit of the nitrogenase enzyme. Discrete seawater samples (2 L) were collected using the TMC-rosette at the same depth as samples for N_2 fixation, filtered using a peristaltic pump onto 0.2 µm Supor (Cole Parmer, Vernon Hills, IL) filters, frozen in liquid nitrogen, and stored at -80°C until processed. The DNA extraction was conducted using published protocols *(22)*. The abundance of *Trichodesmium* spp. was determined using TaqMan qPCR assays with primer-probe sets for *Trichodesmium (23)* as fully described in Turk-Kubo et al., (2015) *(24)*. The same procedures were used for samples collected in the minicosms (see below).

POC export fluxes

A surface tethered drifting mooring line was deployed during the cruise at 10 nm west of Volcano #1 (-21.154; 175.744) for 4 to 5 days and in a distal site not impacted by hydrothermal sources (reference site, -20.394; -166.439) in the South Pacific Gyre (Fig. 1). The line was equipped with C-RESPIRE particle interceptors/incubators at 2 depths: 170 m and 270 m. C-RESPIRE non-intrusively intercepts settling particles colonized by bacteria, and then subsequently incubates them at in situ temperature and pressure conditions within the same device *(25, 26)*. After the particle collection phase, C-RESPIRE provides rates of particle remineralization (predominately by particle-attached bacteria) derived from the change in dissolved oxygen concentration measured by an optode. At the end of the deployment, a triplicate set of aliquots was filtered onto 25-mm diameter pre-combusted (4 h at 450°C) glass microfiber filters (Whatman GF/F), which were subsequently dried for 24 h at 60°C, pelleted and from which particulate organic N (PON), δ^{15}N-PON and C (POC) were analyzed by EA-IRMS (Elemental Analyzer-Isotope Ratio Mass Spectrometry) using an Integra 2 (Sercon) mass spectrometer. The obtained residual POC fluxes were corrected for bacterial remineralization using O_2 consumption rates and a C:O_2 conversion factor (117/170 (*27*)) to provide reconstructed POC fluxes.

Another fixed mooring line was also deployed for one year in the fertilized patch (Station 12: -20.702; -177.866). The mooring line was instrumented with a Technicap PPS5 (1 m^2 collecting area, aspect ratio (height/width) of 5.2) sediment trap and inclinometer (NKE S2IP) at a depth of 1000 m (seafloor depth 2000 m). A conductivity–temperature–pressure (CTD) sensor (Sea-Bird SBE 37) and a current meter (Nortek Aquadopp) were placed on the mooring line 35 m beneath the sediment trap. The sediment trap collection period started on 2 December 2019 and continued until 18 October 2020. The sediment trap was composed of 24 rotating sample cups (250 mL) filled with a 5% formalin hypersaline solution buffered with sodium tetraborate at pH 8. Rotation of the carousel was programmed to sample short intervals of 13.9 days. Samples were treated following the standard JGOFS' protocol (as described in Guieu et al., 2005 *(28)*). Total carbon, particulate organic carbon (POC) (after removing inorganic carbon by acidification with HCl 2N), were measured on a CHN elemental analyzer (2400 Series II CHNS/O Elemental Analyzer, Perkin Elmer).

Nitrate+Nitrate isotope analysis

The isotopic analysis of nitrate+nitrite was conducted at Florida State University in the Knapp Laboratory. The δ^{15}N of nitrate+nitrite was determined using the "denitrifier" method *(29, 30)*. The δ^{15}N of nitrate+nitrite was analyzed using a continuous flow ThermoFisher Delta V

Advantage IRMS interfaced with a Gasbench II *(29, 31)*. International reference materials including IAEA-NO_3 and USGS34 were included in all runs to allow for isotopic calibration. This analysis was performed on nitrate+nitrite samples with concentrations >1.0 µM. Using this method, we report $\delta^{15}N$ nitrate+nitrite values with a SD of <0.2‰.

Mixing experiment with increasing additions of hydrothermally-enriched seawater

Mixing experiments were performed tanks installed in a clean, temperature-controlled container (Fig. S7A). The tanks were made of high-density polyethylene (HDPE) and were trace-metal-free in order to avoid contaminations, with a height of 1.09 m, a diameter of 0.68 m, a surface area of 0.36 m^2 and a volume of 0.3 m^3 (300 L). Each tank was equipped with a lid containing six rows of LEDs (Alpheus©). Each of these rows were composed of blue, green, cyan and white units in order to mimic the natural sun spectrum. Photosynthetically active radiation (PAR; 400–700 nm) and temperature were continuously monitored in each tank using respectively QSL-2100 Scalar PAR Irradiance Sensors (Biospherical Instruments©) and pt1000 temperature sensors (Metrohm©) connected to a D230 datalogger (Consort©).

On November 11th 2019, five tanks were filled under trace metal clean conditions using a high-speed peristaltic pump (Verder© VF40, flow of 1200 L h^{-1}) *(32)* with surface seawater (~5 m) sampled East of the Tonga arc (-21.692; -174.854W), outside of the influence of volcanic activity. After homogeneously filling all tanks up to 275 L (performed within 2 h), one tank was immediately sampled and emptied in order to characterize the biogeochemical conditions in the surface water end-member before mixing. Upon arrival at the Volcano #1 station, hydrothermally-enriched_seawater was pumped at ~200 m where the maximal acoustic signal was recorded (see main text), using the same protocol as previously described and stored in the tank that had been previously emptied. From this tank, after sampling for the initial characterization of the hydrothermal fluid, precise volumetric additions were performed in each experimental tank following the removal of the corresponding surface water in order to maintain a final volume of 275 L in all tanks. We added increasing amounts of hydrothermally-enriched water: 0% (Control) to 1.8%, 5.5% and 14.5% in volume. Sampling was performed 12h, 24h, 48h, 96h, 144h and 216h after mixing for pH, DFe, nitrate and phosphate concentrations. The biological response of diazotrophs (N_2 fixation rates and *Trichodesmium* abundances) was measured after 48h, 96h, 144h and 196h.

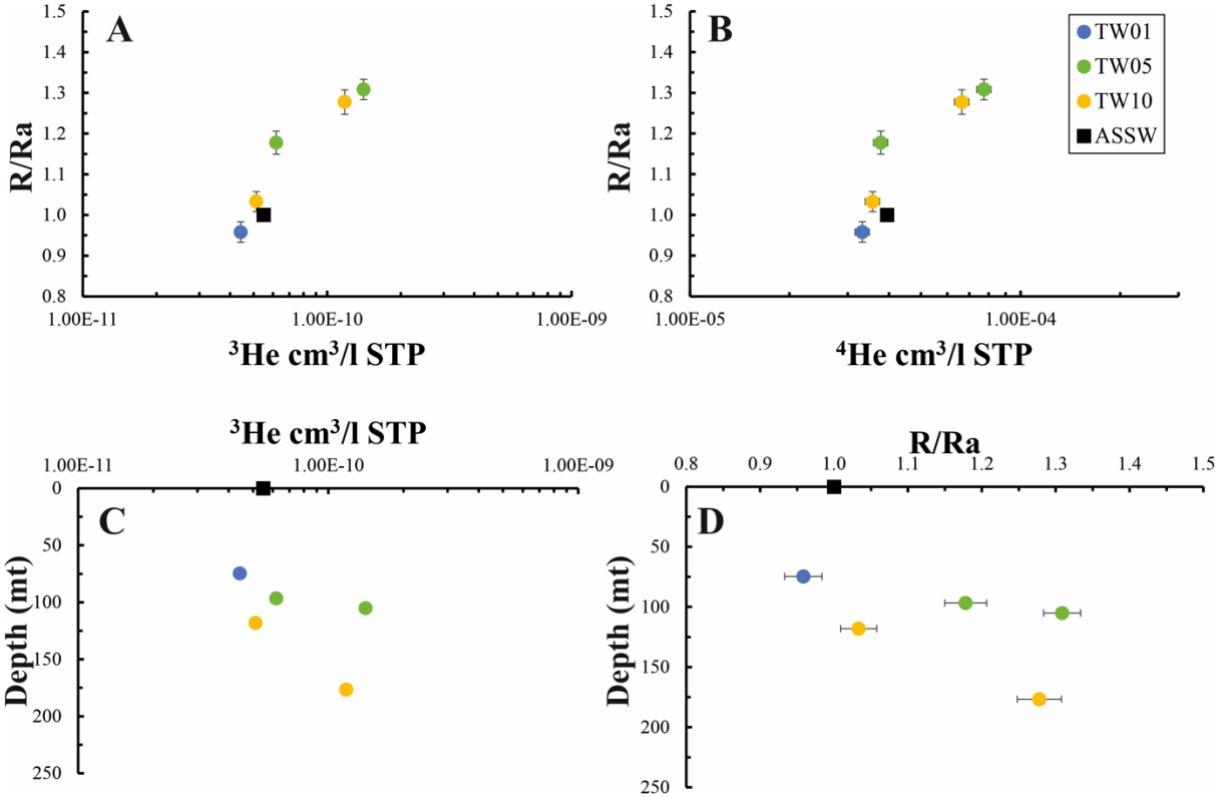

Fig. S1. He analyses above Volcano #1. R/Ra values vs concentrations in cc/l STP (Standard Temperature and Pressure) of ^{3}He (A) and ^{4}He (B) in water samples from three distinct vertical profiles performed above Volcano #1. Air Saturated Sea Water (ASSW) is also reported for comparison. The ^{3}He concentration and R/Ra values are also plotted vs the sampling depth.

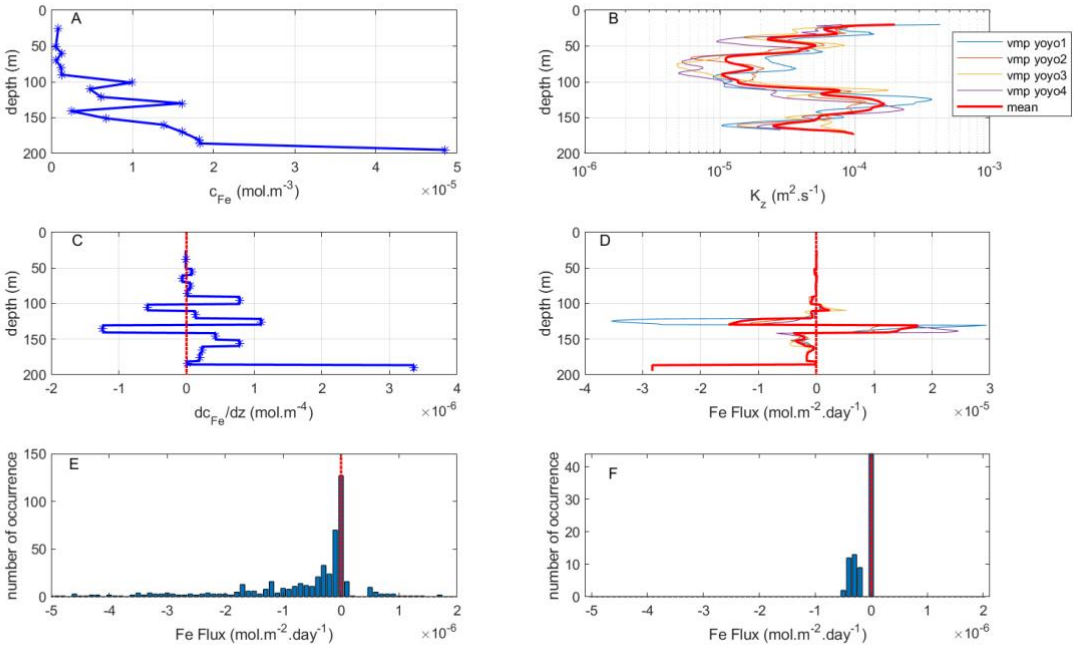

Fig. S2. Station above Volcano #1 (A) Dissolved Fe (DFe) concentrations, C_{Fe} (B) Vertical eddy diffusivity, Kz (C) Vertical gradient of DFe, dc_{Fe}/dz. (D) DFe turbulent diffusive flux (the red line corresponds to the mean flux). (E & F) Histogram of DFe turbulent diffusive fluxes calculated step by step along the whole vertical profile (E) and at the base of the mixed layer (F) showing that most values are indicative of upward diffusive fluxes.

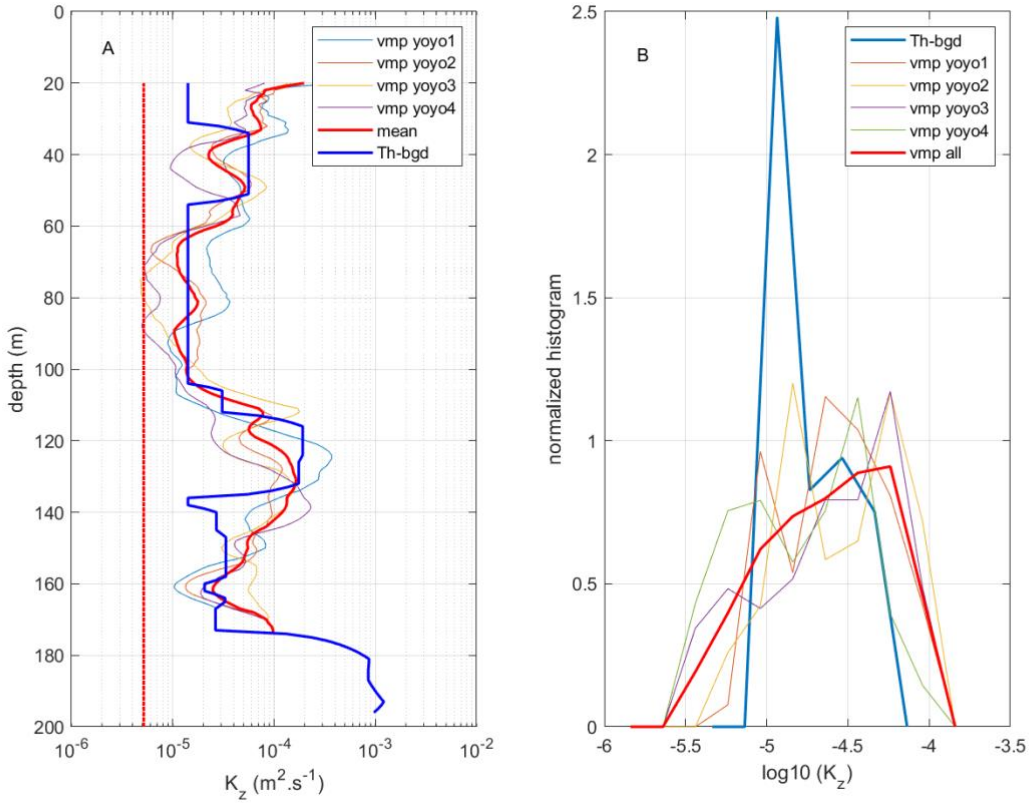

Fig. S3. Validation of the indirect estimate of vertical eddy diffusivity from CTD at Volcano 1: (A) Measured averaged Kz profile at Volcano 1 (red), and estimated Kz from CTD (cyan), individual VMP profiles (thin colored curves). The constant value for a background internal wave far from sources and sinks is shown with a vertical red line. (B) Normalized histograms of vertical eddy diffusivity (log10), indirect estimate from CTD (blue), all VMP data (red), individual profiles (thin colored curves).

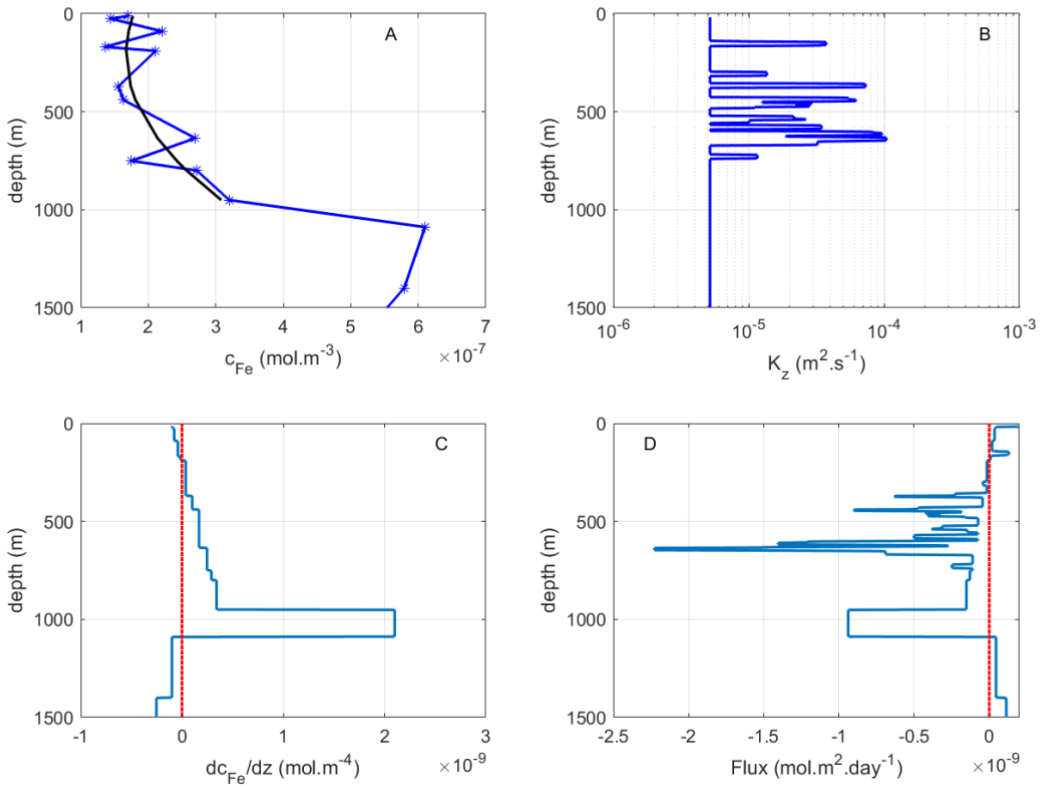

Fig. S4. Reference site (gyre) (A) Dissolved iron concentrations, c_{Fe} (B) Vertical eddy diffusivity estimate, Kz, (C) Vertical gradient of DFe, dc_{Fe}/dz. (D) DFe turbulent diffusive flux.

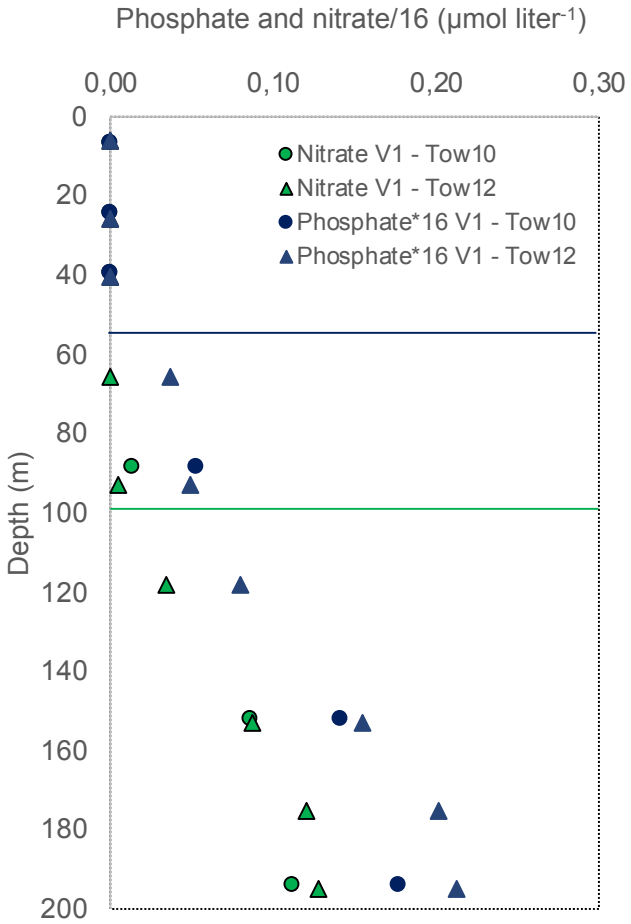

Fig. S5. Nutrient concentrations above Volcano #1. Nitrate (green symbols) and phosphate (dark blue symbols) concentrations (x16 to plot them on the same scale) measured above Volcano #1 during the tow-yo survey, and showing the decoupling between the depth of the nitracline (~100 m) and that of the phosphacline (50-60 m).

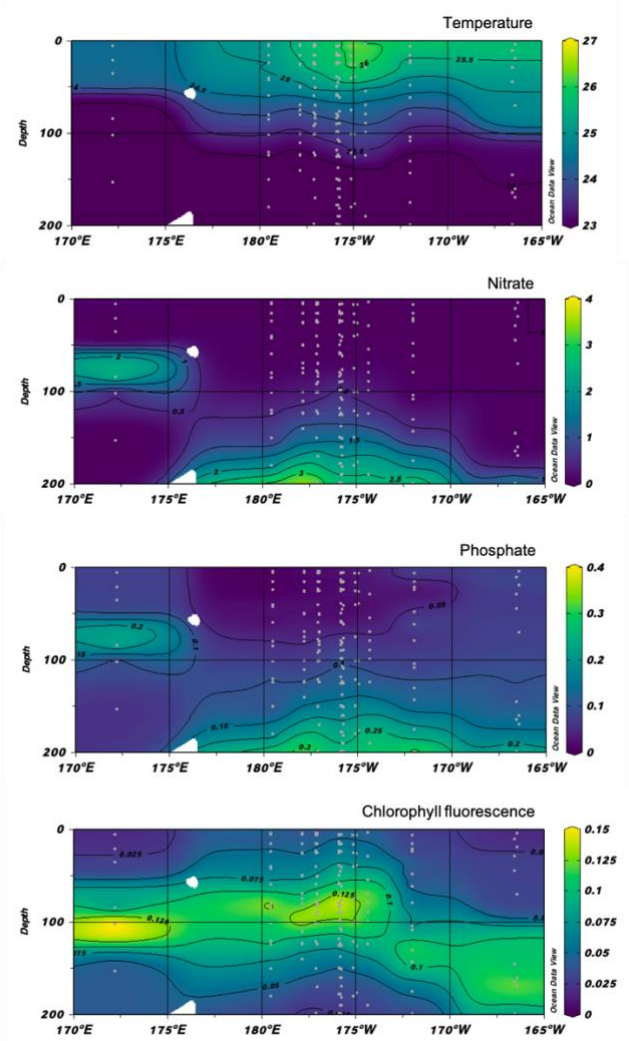

Fig. S6. Horizontal and vertical distributions physico-chemical parameters during the TONGA transect. A. Seawater temperature (°C), B. nitrate concentrations (µmol liter^{-1}), C. phosphate concentrations (µmol liter^{-1}) and D. Chlorophyll Fluorescence, across the TONGA transect. Y axis: pressure (dbar), X axis: longitude; grey dots correspond to sampling depths at the various stations.

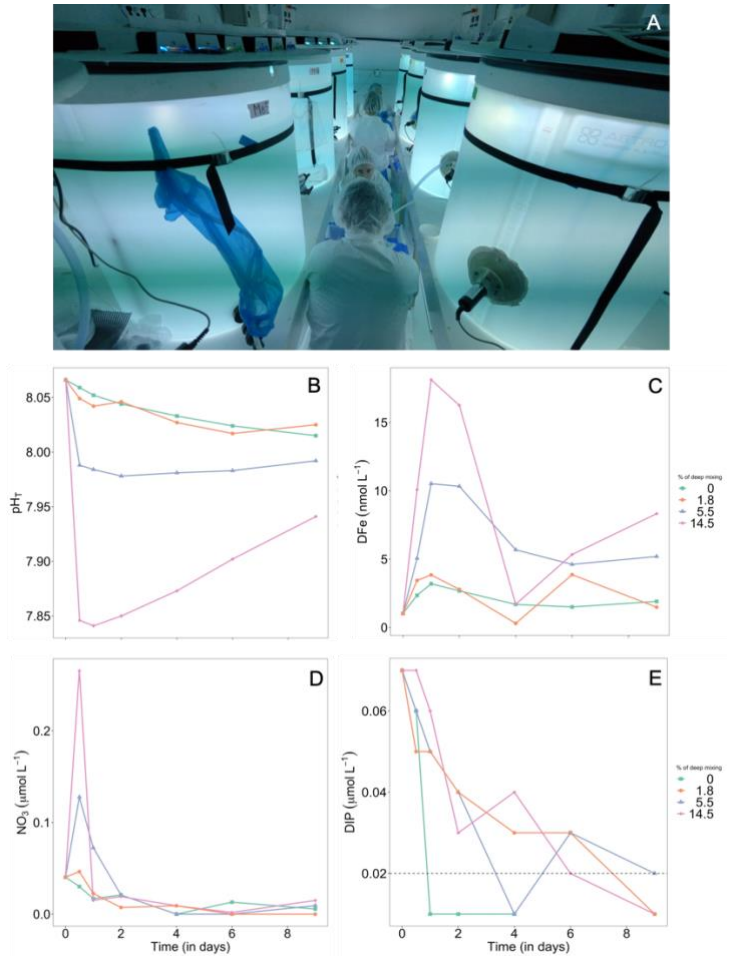

Fig. S7. (A) Picture showing the experimental 300-L reactors inside the trace metal clean van onboard. **Temporal evolution of** (B) pH, (C) DFe concentrations, (D) Nitrate concentrations, and (E) Dissolved Inorganic Phosphorus (DIP) concentrations during the minicosm experiments. The T0 corresponds to the values measured before mixing in ambient seawater.

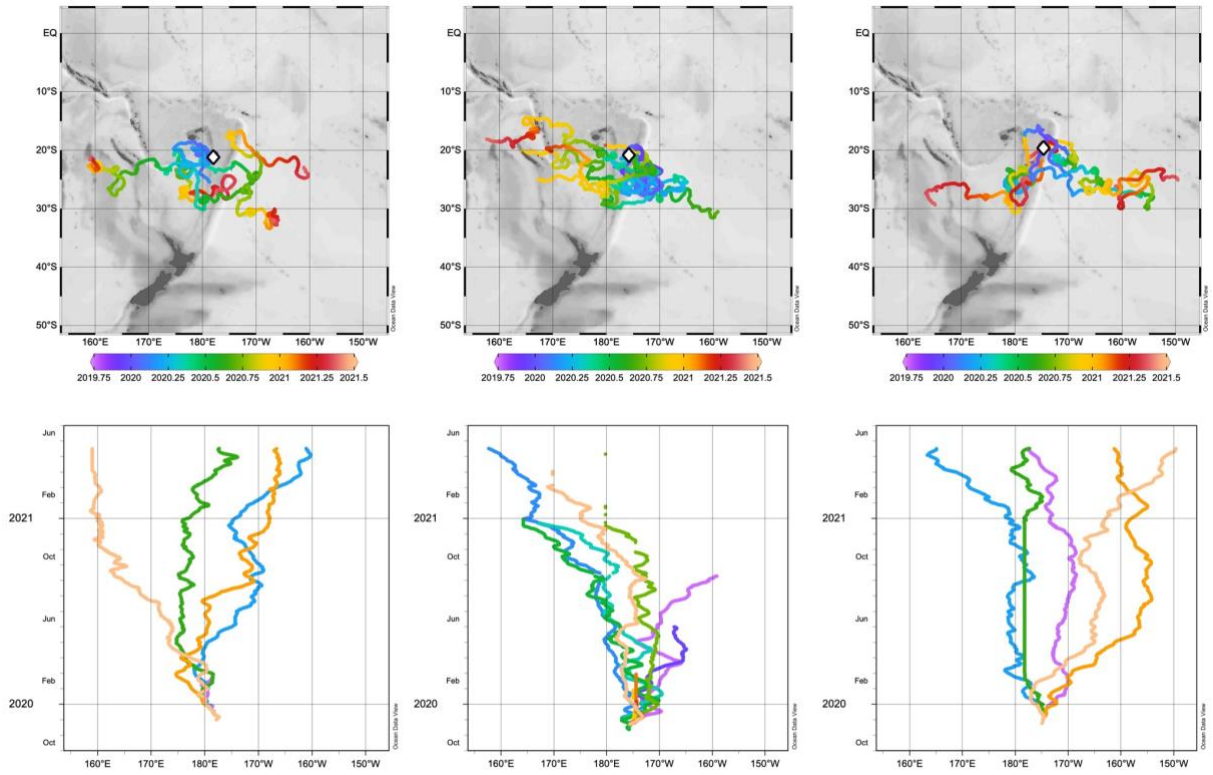

Fig. S8. 20 months trajectories of SVP drifters deployed at Volcano #1 (middle panels) and two adjacent sites in the Lau Basin (left and right panels) during the TONGA cruise. The three clusters of deployment (5 drifters per cluster) are indicated by the white diamonds. Lower panels: zonal dispersion of each cluster during the 20 months.

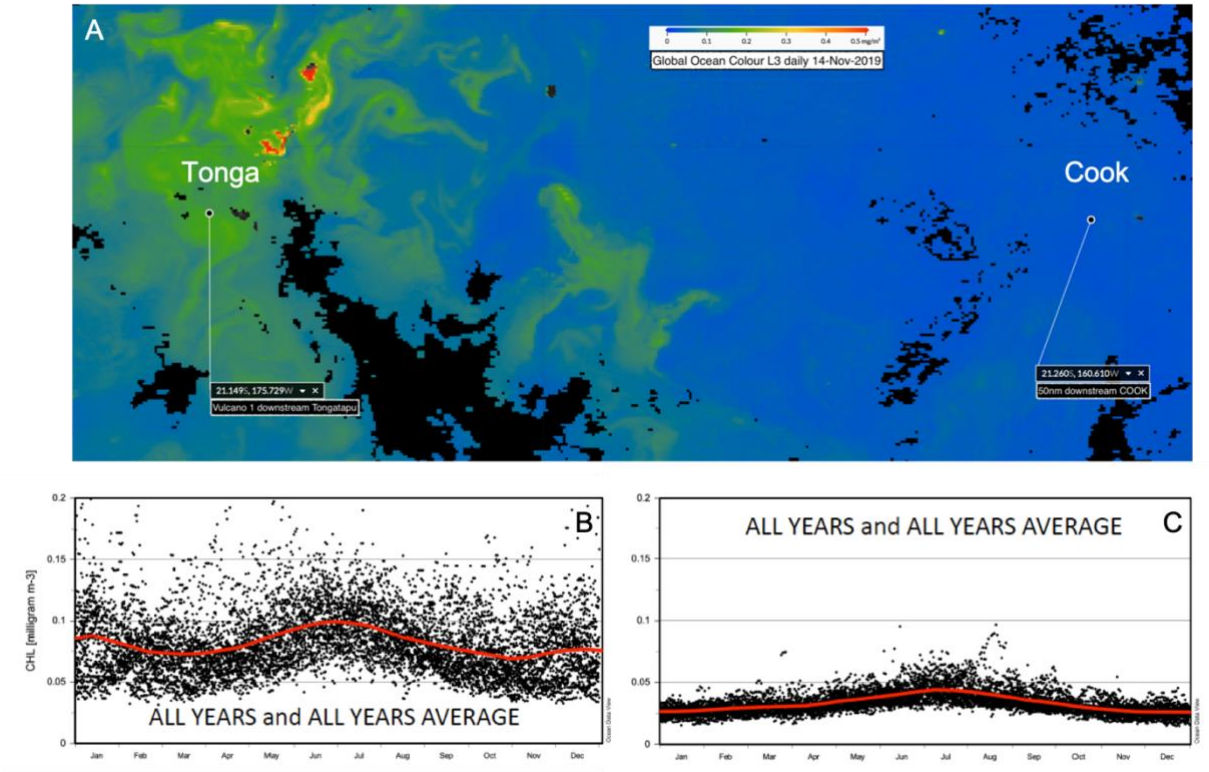

Fig. S9. Chl*a* concentrations in the vicinity of the Tonga and Cook archipelagos. (A) Surface [Chl*a*] in November 2019, (B) Monthly climatology of [Chl*a*] from a 23 years-time series (1997-2020, GLOBCOLOR product) 50 km west of Tonga main island, and (C) 50 km west of Cook main island (right) for comparison. Data show that despite identical annual precipitation, no perceptible increase of Chl*a* occurs around Cook.

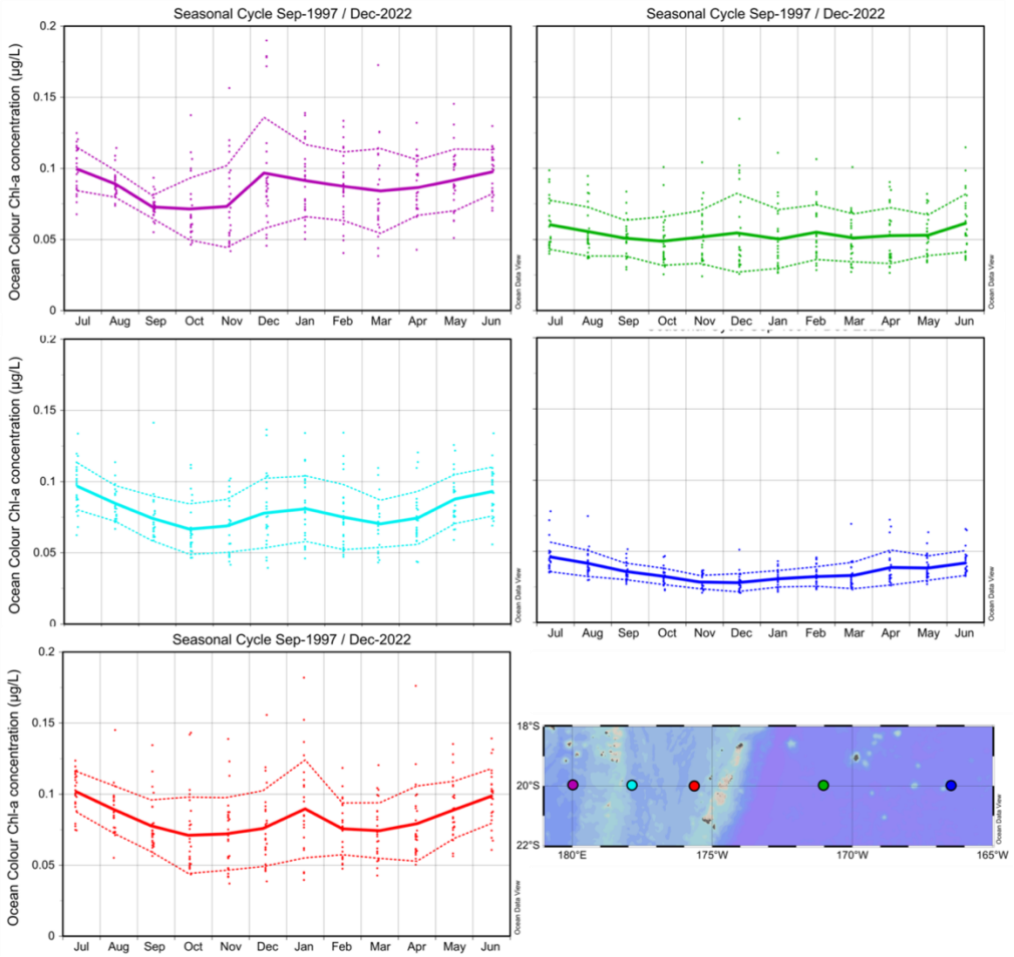

Fig. S10. 25-years' time series of Chl*a* concentration seasonal cycles in the WTSP. Data are derived from 25-years monthly "cloud free" Copernicus-GLOBCOLOUR database, at five zonal locations along 20°S. Every values indicated in dots, mean values for each month indicated in bold lines, associated standard deviation in dotted lines.

Table S1. Position of the detected acoustic plumes during the bathymetric survey above Volcano #1.

ID	LAYER_EM710_file (processed)	PING	LATITUDE_DEG	LONGITUDE_DEG	LATITUDE_DMD	LONGITUDE_DMD	SEA_FLOOR_ELEVATION (m)	DATE	TIME	GROUP	Active site
1	0011_20191108_204355_ATL_v20220919_Raw_PolarEchograms.xml	527	-21,1451051	-175,757274	-21 8,700	-175 45,433	-161,942	08/11/2019	21:08:30	FLUID	near to Stoffer_el_al_2006 dive site
2	0011_20191108_204355_ATL_v20220919_Raw_PolarEchograms.xml	538	-21,1442623	-175,758121	-21 8,650	-175 45,483	-131,984	08/11/2019	21:09:05	FLUID	near to Stoffer_el_al_2006 dive site
3	0011_20191108_204355_ATL_v20220919_Raw_PolarEchograms.xml	550	-21,1435306	-175,7592774	-21 8,617	-175 45,550	-141,841	08/11/2019	21:09:40	FLUID	near to Stoffer_el_al_2006 dive site
4	0011_20191108_204355_ATL_v20220919_Raw_PolarEchograms.xml	560	-21,1424416	-175,7594387	-21 8,550	-175 45,567	-129,742	08/11/2019	21:10:11	FLUID	near to Stoffer_el_al_2006 dive site
5	0014_20191108_212226_ATL_v20220919_Raw_PolarEchograms.xml	185	-21,1432325	-175,7594255	-21 8,600	-175 45,567	-132,973	08/11/2019	21:30:58	FLUID	near to Stoffer_el_al_2006 dive site
6	0014_20191108_212226_ATL_v20220919_Raw_PolarEchograms.xml	194	-21,1434288	-175,7576415	-21 8,600	-175 45,467	-101,007	08/11/2019	21:31:17	FLUID	near to Stoffer_el_al_2006 dive site
7	0014_20191108_212226_ATL_v20220919_Raw_PolarEchograms.xml	200	-21,1441304	-175,7581634	-21 8,650	-175 45,483	-128,335	08/11/2019	21:31:32	FLUID	near to Stoffer_el_al_2006 dive site
8	0014_20191108_212226_ATL_v20220919_Raw_PolarEchograms.xml	205	-21,1442482	-175,7571829	-21 8,650	-175 45,433	-123,773	08/11/2019	21:31:44	FLUID	near to Stoffer_el_al_2006 dive site
9	0014_20191108_212226_ATL_v20220919_Raw_PolarEchograms.xml	209	-21,1446603	-175,7573117	-21 8,683	-175 45,433	-140,65	08/11/2019	21:31:54	FLUID	near to Stoffer_el_al_2006 dive site
10	0014_20191108_212226_ATL_v20220919_Raw_PolarEchograms.xml	214	-21,1451478	-175,7572592	-21 8,717	-175 45,433	-164,198	08/11/2019	21:32:07	FLUID	near to Stoffer_el_al_2006 dive site
11	0016_20191108_214138_ATL_v20220919_Raw_PolarEchograms.xml	137	-21,1434942	-175,7561255	-21 8,617	-175 45,367	-140,103	08/11/2019	21:47:39	FLUID	near to Stoffer_el_al_2006 dive site
12	0016_20191108_214138_ATL_v20220919_Raw_PolarEchograms.xml	145	-21,1434263	-175,7578984	-21 8,600	-175 45,467	-95,867	08/11/2019	21:47:58	FLUID	near to Stoffer_el_al_2006 dive site
13	0016_20191108_214138_ATL_v20220919_Raw_PolarEchograms.xml	161	-21,142168	-175,7581842	-21 8,533	-175 45,483	-118,765	08/11/2019	21:48:34	FLUID	near to Stoffer_el_al_2006 dive site
14	0022_20191108_225737_ATL_v20220919_Raw_PolarEchograms.xml	324	-21,1587724	-175,7458361	-21 9,533	-175 44,750	-88,826	08/11/2019	23:11:04	FLUID	Western flank of PANAMAX volcanic structure
15	0024_20191108_232523_ATL_v20220919_Raw_PolarEchograms.xml	263	-21,1586999	-175,7454203	-21 9,517	-175 44,733	-88,307	08/11/2019	23:36:53	FLUID	Western flank of PANAMAX volcanic structure
16	**0026_20191108_235803_ATL_v20220919_Raw_PolarEchograms.xml**	**321**	**-21,1540043**	**-175,7446121**	**-21 9,233**	**-175 44,683**	**-202,423**	**09/11/2019**	**00:11:28**	**FLUID**	**PANAMAX (TONGA expedition sampling site)**
17	**0026_20191108_235803_ATL_v20220919_Raw_PolarEchograms.xml**	**322**	**-21,1541143**	**-175,7446859**	**-21 9,250**	**-175 44,683**	**-203,102**	**09/11/2019**	**00:11:30**	**FLUID**	**PANAMAX (TONGA expedition sampling site)**
18	**0026_20191108_235803_ATL_v20220919_Raw_PolarEchograms.xml**	**322**	**-21,154186**	**-175,7448504**	**-21 9,250**	**-175 44,683**	**-203,332**	**09/11/2019**	**00:11:30**	**FLUID**	**PANAMAX (TONGA expedition sampling site)**
19	**0026_20191108_235803_ATL_v20220919_Raw_PolarEchograms.xml**	**322**	**-21,154186**	**-175,7448504**	**-21 9,250**	**-175 44,683**	**-203,332**	**09/11/2019**	**00:11:30**	**FLUID**	**PANAMAX (TONGA expedition sampling site)**
20	**0026_20191108_235803_ATL_v20220919_Raw_PolarEchograms.xml**	**327**	**-21,1543594**	**-175,7442353**	**-21 9,267**	**-175 44,650**	**-201,724**	**09/11/2019**	**00:11:42**	**FLUID**	**PANAMAX (TONGA expedition sampling site)**
21	**0026_20191108_235803_ATL_v20220919_Raw_PolarEchograms.xml**	**326**	**-21,1545502**	**-175,7448835**	**-21 9,267**	**-175 44,700**	**-200,199**	**09/11/2019**	**00:11:39**	**FLUID**	**PANAMAX (TONGA expedition sampling site)**
22	**0026_20191108_235803_ATL_v20220919_Raw_PolarEchograms.xml**	**330**	**-21,1547013**	**-175,744383**	**-21 9,283**	**-175 44,667**	**-200,597**	**09/11/2019**	**00:11:48**	**FLUID**	**PANAMAX (TONGA expedition sampling site)**
23	0040_20191109_033432_ATL_v20220919_Raw_PolarEchograms.xml	53	-21,1571767	-175,7461368	-21 9,433	-175 44,767	-101,239	09/11/2019	03:40:03	FLUID	Western flank of PANAMAX volcanic structure
24	0040_20191109_033432_ATL_v20220919_Raw_PolarEchograms.xml	53	-21,157695	-175,745431	-21 9,467	-175 44,733	-88,285	09/11/2019	03:40:03	FLUID	Western flank of PANAMAX volcanic structure
25	**0040_20191109_033432_ATL_v20220919_Raw_PolarEchograms.xml**	**71**	**-21,1548679**	**-175,7443148**	**-21 9,300**	**-175 44,667**	**-198,359**	**09/11/2019**	**03:41:24**	**FLUID**	**PANAMAX (TONGA expedition sampling site)**
26	**0040_20191109_033432_ATL_v20220919_Raw_PolarEchograms.xml**	**72**	**-21,1546396**	**-175,7443932**	**-21 9,283**	**-175 44,667**	**-202,306**	**09/11/2019**	**03:41:28**	**FLUID**	**PANAMAX (TONGA expedition sampling site)**
27	**0040_20191109_033432_ATL_v20220919_Raw_PolarEchograms.xml**	**75**	**-21,1541622**	**-175,7443342**	**-21 9,250**	**-175 44,667**	**-202,309**	**09/11/2019**	**03:41:42**	**FLUID**	**PANAMAX (TONGA expedition sampling site)**
28	**0040_20191109_033432_ATL_v20220919_Raw_PolarEchograms.xml**	**75**	**-21,1542392**	**-175,7442198**	**-21 9,250**	**-175 44,650**	**-201,268**	**09/11/2019**	**03:41:42**	**FLUID**	**PANAMAX (TONGA expedition sampling site)**

Table S2. Discrete measurements of optical and physico-chemical characteristics (Eh, pH, temperature, salinity, CH_4, DIC, DFe, DMn, nitrate and phosphate concentrations) at the 'Panamax site' above Volcano #1.

Lat	Long	Depth (m)	Eh (mV)	pH	Temperature (°C)	Salinity	CH4 (nmol liter-1)	DIC (µmol liter-1)	Fe (nmol liter-1)	SD_Fe	Mn (nmol liter-1)	Nitrate (µmol liter-1)	Phosphate (µmol liter-1)
-21.15454	-175.7444	195	-676,7	6,96	21,32	35,66	104,1	2222,48	48,5	0,068		2,04	0,21
-21.15454	-175.74438	186	-691,5	6,97	21,23	35,65	44,5		18,3	0,088	33,23		
-21.15456	-175.74438	181	-404,5	7,03	21,39	35,65	40,7		18,3	0,09	35,28		
-21.15456	-175.74438	170	344,5	7,62	21,77	35,63	26,8	2188,19	16,1	0,024	20,15	1,93	0,20
-21.15456	-175.7444	160	353,25	7,78	21,91	35,62			13,8	0,024	17,56		
-21.15456	-175.7444	151	366,25	7,87	22,47	35,51	2,6	2161,56	6,8	0,016	5,73	1,39	0,15
-21.15454	-175.74438	141	385,5	7,9	22,64	35,46			2,5	0,044	1,28		
-21.15454	-175.74439	130	384,75	7,88	22,07	35,57			16,1	0,024	0,02		
-21.15454	-175.7444	121	385,5	7,9	22,94	35,38	3,8	2232,86	6,2	0,008	0,02	0,55	0,08
-21.15456	-175.7444	110	377,75	7,91	22,94	35,38			4,7	0,078	0,02		
-21.15456	-175.7444	101	366,25	7,89	23,21	35,36			9,9	0,078	0,02		
-21.15456	-175.7444	90	317	7,9	23,62	35,38		2845,21	1,3	0,095	0,01	0,06	0,05
-21.15456	-175.7444	80	295,55	7,9	23,92	35,29			1,2	0,012	0,4		
-21.15456	-175.7444	70	285,25	7,9	24,23	35,26	9,8	1914,27	0,6	0,051	0,41	<LQ	0,04
-21.15456	-175.7444	60	294,25	7,9	24,44	35,24			1,3	0,082	1,03		
-21.15456	-175.7444	51	304,25	7,9	24,79	35,21			0,6	0,062	0,99	<LQ	<LQ
-21.15456	-175.7444	25	321	8,02	24,88	35,44	3,8	2349,86	0,9	0,012	0,84	<LQ	<LQ
-21.15456	-175.7444	5										<LQ	<LQ

Table S3. Mean values and standard deviations of vertical eddy diffusivity, vertical gradient of DFe and turbulent diffusive flux of DFe at the base of the mixed layer (where most biological biomass accumulates) above Volcano #1 and at the reference site. Values in italic of standard deviations are computed over the euphotic layer when no variations at the base of the mixed layer.

	Above Volcano #1			**Reference site**		
Depth	Kz $m^2 s^{-1}$	Dc/dz mol m^{-4}	Flux mol m^{-2} d^{-1}	Kz $m^2 s^{-1}$	Dc/dz mol m^{-4}	Flux mol m^{-2} d^{-1}
40m-60m	$3.68x10^{-5}$ $\pm 1.91x10^{-5}$	$3.12x10^{-8}$ $\pm 4.71x10^{-8}$	$-1.06x10^{-7}$ $\pm 1.68x10^{-7}$	$5.17x10^{-6}$ *$\pm 9.66x10^{-6}$*	$7.75x10^{-11}$ *$\pm 3.08x10^{-11}$*	$3.46x10^{-11}$ *$\pm 3.08x10^{-11}$*

Table S4. Mean values and standard deviations of vertical gradient of nitrate, phosphate and silicate and their turbulent diffusive fluxes at the base of the mixed layer above Volcano #1

Depth	Nitrate Dc/dz mol m^{-4}	Nitrate flux mol m^{-2} d^{-1}	Phosphate Dc/dz mol m^{-4}	Phosphate flux mol m^{-2} d^{-1}	Silicate Dc/dz- mol m^{-4}	Silicate flux mol m^{-2} d^{-1}
40m-60m	0	**0**	$1.60x10^{-6} \pm 0$	$-5.43x10^{-6}$ $\pm 2.38x10^{-6}$	$1.20x10^{-6} \pm 0$	$-4.07x10^{-6} \pm 1.78x10^{-6}$

Table S5. Comparison of POC export fluxes (mmol C m^{-2} d^{-1}) measured at the base of the euphotic zone in different (sub)tropical regions where diazotrophs are present. It should be noted that different collection time, and different instruments used preclude a strict comparison of the data.

	POC mmol C m^{-2} d^{-1}	Reference
South Pacific gyre	0.3±0.1	Caffin et al., (2018) (*33*) (from drifting conical traps at 150 m, average of 5 days)
Eastern Mediterranean Sea	0.4±0.3	Alkalay et al., (2020) (*34*) (from fixed cylindrical traps at 180 m, average of 6 months)
Western Mediterranean Sea	0.9±1.0	Ternon et al., (2010) (*35*) (from fixed conical traps at 200 m, average of a 4 years time-series)
WTSP (outside hydrothermal influence)	1.4 -1.7	This study (from drifting cylindrical traps at Station 8 at 170 & 270 m, average of 5 days)
Subtropical North Atlantic (BATS-BIOS)	2.3±1.2	Karl et al., (2003) (*36*), Lomas et al., (2022) (*37*) (from drifting cylindrical traps at 150 m, average of a 30-years time series)
Subtropical North Pacific (ALOHA)	2.3±0.8	Karl et al., (2021) (*38*) (from drifting cylindrical traps at 150 m, average of a 30-years time series)
WTSP (inside hydrothermal influence)	3.2 -3.9	This study (from drifting cylindrical traps at Station 5 at 170 & 270 m, average of 5 days)

Table S6. Physico-chemical characteristics (pH, DFe, nitrate and phosphate concentrations) of the endmember fluid used for the trace metal clean enrichment experiments in 300L-reactors.

	Endmember fluid	Surface seawater
pH	6.4	8.1
DFe (nmol liter^{-1})	15.8	1.0
Nitrate (µmol liter^{-1})	2.01	0.05
Phosphate (µmol liter^{-1})	0.23	0.07

Table S7. Temporal evolution of *Trichodesmium* abundances (*nifH* gene copies L^{-1}) and N_2 fixation rates (nmol N L^{-1} d^{-1}) along the 196h minicosm experiment in the control treatment (no fluid addition), and in the reactors amended with 1.8%, 5.5%, and 14.5% of 'plume water' collected at the 'Panamax site' of Volcano #1 (~200 m depth).

Sampling time	% 'plume water' added	Tichoodesmium (*nifH* copies L^{-1})	SD	N_2 fixation rates (nmol N L^{-1} d^{-1})	SD
48h	0	2,0E+04	6,8E+03	1,9	0,1
48h	5,5	6,8E+04	2,1E+04	3,9	0,2
48h	14,5	4,2E+04	9,1E+03	7,8	0,4
48h	1,8	2,8E+04	7,4E+03	11,9	0,6
96h	0	2,8E+04	1,0E+04	0,8	0,1
96h	5,5	1,1E+05	7,7E+04	11,6	0,6
96h	14,5	7,7E+04	2,1E+04	9,2	0,4
96h	1,8	6,7E+04	1,3E+04	4,5	0,2
144h	0	1,2E+04	2,6E+03	0,4	0,1
144h	5,5	6,3E+04	6,2E+03	5,1	0,3
144h	14,5	5,0E+04	1,3E+04	3,7	0,2
144h	1,8	1,7E+05	1,3E+04	3,5	0,2
196h	0	2,3E+03	2,4E+02	0,3	0,1
196h	5,5	5,8E+03	5,3E+03	0,3	0,1
196h	14,5	2,5E+03	2,1E+03	1,7	0,1
196h	1,8	8,5E+03	1,2E+03	1,6	0,1

References cites

1. W. W. Chadwick *et al.*, Imaging of CO2 bubble plumes above an erupting submarine volcano, NW Rota-1, Mariana Arc. *Geochem Geophy Geosy* **15**, 4325-4342 (2014).
2. J. M. Augustin, 2023. SonarScope software. SEANOE. https://doi.org/10.17882/87777.
3. C. B. Poncelet, G., Corre, M.P. (2023). Globe (GLobal Oceanographic Bathymetry Explorer) Software . SEANOE . https://doi.org/10.17882/70460.
4. K. G. Foote, H. P. Knudsen, G. Vestnes, Calibration of Acoustic Instruments for Fish Density-Estimation - a Practical Guide. *J Acoust Soc Am* **83**, 831-832 (1988).
5. Y. Sano, T. P. Fischer, in *The noble gases as geochemical tracers*. (Springer, 2013), pp. 249-317.
6. W. Aeschbach-Hertig, D. K. Solomon, Noble gas thermometry in groundwater hydrology. *The noble gases as geochemical tracers*, 81-122 (2013).
7. A. L. Rizzo *et al.*, Kolumbo submarine volcano (Greece): An active window into the Aegean subduction system. *Scientific Reports* **6**, (2016).
8. C. Tilliette *et al.*, Dissolved Iron Patterns Impacted by Shallow Hydrothermal Sources Along a Transect Through the Tonga-Kermadec Arc. *Global Biogeochemical Cycles* **36**, e2022GB007363 (2022).
9. M. Tonnard *et al.*, Dissolved iron in the North Atlantic Ocean and Labrador Sea along the GEOVIDE section (GEOTRACES section GA01). *Biogeosciences* **17**, 917-943 (2020).
10. P. Bouruet-Aubertot *et al.*, Longitudinal contrast in turbulence along a similar to 19 degrees S section in the Pacific and its consequences for biogeochemical fluxes. *Biogeosciences* **15**, 7485-7504 (2018).
11. T. R. Osborn, Estimates of the Local-Rate of Vertical Diffusion from Dissipation Measurements. *J Phys Oceanogr* **10**, 83-89 (1980).
12. T. M. Dillon, Vertical Overturns - a Comparison of Thorpe and Ozmidov Length Scales. *J Geophys Res-Oceans* **87**, 9601-9613 (1982).
13. S. A. Thorpe, Turbulence and Mixing in a Scottish Loch. *Philos T R Soc A* **286**, 125-181 (1977).
14. E. Kunze, E. Firing, J. M. Hummon, T. K. Chereskin, A. M. Thurnherr, Global abyssal mixing inferred from lowered ADCP shear and CTD strain profiles (vol 36, pg 1553, 2006). *J Phys Oceanogr* **36**, 2350-2352 (2006).
15. A. Aminot, R. Kerouel, Quae, Ed. (2007), pp. 187 pp.
16. S. Bonnet *et al.*, In-depth characterization of diazotroph activity across the western tropical South Pacific hotspot of N-2 fixation (OUTPACE cruise). *Biogeosciences* **15**, 4215-4232 (2018).
17. I. Klawonn *et al.*, Simple approach for the preparation of 15−15N2-enriched water for nitrogen fixation assessments: evaluation, application and recommendations. *Frontiers in microbiology* **6**, (2015).
18. M. Benavides, H. Berthelot, S. Duhamel, P. Raimbault, S. Bonnet, Dissolved organic matter uptake by Trichodesmium in the Southwest Pacific. *Scientific Reports* **7**, 41315 (2017).

19. P. H. Moisander *et al.*, Analogous nutrient limitations in unicellular diazotrophs and *Prochlorococcus* in the South Pacific Ocean. *The ISME journal* **6**, 733-744 (2011).
20. J. P. Montoya, M. Voss, P. Kahler, D. G. Capone, A simple, high-precision, high-sensitivity tracer assay for N_2 fixation. *Applied and Environmental Microbiology* **62**, 986-993 (1996).
21. T. M. Kana *et al.*, A membrane inlet mass spectrometer for rapid high precision determination of N_2, O_2, and Ar in environmental water samples. *Analytical Chemistry* **66**, 4166–4170 (1994).
22. A. M. Moisander, A. Beinart, M. Voss, J. P. Zehr, Diversity and abundance of diazotrophs in the South China Sea during intermonsoon. *The ISME journal* **2**, 954-967 (2008).
23. M. J. Church, B. D. Jenkins, D. M. Karl, J. P. Zehr, Vertical distributions of nitrogen-fixing phylotypes at Stn ALOHA in the oligotrophic North Pacific Ocean. *Aquatic Microbial Ecology* **38**, 3-14 (2005).
24. K. A. Turk-Kubo *et al.*, Diazotroph community succession during the VAHINE mesocosms experiment (New Caledonia Lagoon). *Biogeosciences* **12**, 7435-7452 (2015).
25. P. W. Boyd, A. McDonnell, J. Valdez, D. LeFevre, M. P. Gall, RESPIRE: An in situ particle interceptor to conduct particle remineralization and microbial dynamics studies in the oceans' Twilight Zone. *Limnol Oceanogr-Meth* **13**, 494-508 (2015).
26. M. Bressac *et al.*, Resupply of mesopelagic dissolved iron controlled by particulate iron composition. *Nature Geoscience* **12**, 995-+ (2019).
27. L. A. Anderson, J. L. Sarmiento, Redfield Ratios of Remineralization Determined by Nutrient Data-Analysis. *Global Biogeochemical Cycles* **8**, 65-80 (1994).
28. C. Guieu *et al.*, Vertical particle flux in the northeast Atlantic Ocean (POMME experiment). *J Geophys Res-Oceans* **110**, (2005).
29. K. L. Casciotti, D. M. Sigman, M. G. Hastings, J. K. Böhlke, A. Hilkert, Measurement of the Oxygen Isotopic Composition of Nitrate in Seawater and Freshwater Using the Denitrifier Method. *Analytical Chemistry* **74**, 4905–4912 (2002).
30. D. M. Sigman *et al.*, A bacterial method for the nitrogen isotopic analysis of nitrate in seawater and freshwater. *Analytical Chemistry* **73**, 4145–4153 (2001).
31. M. R. McIlvin, K. L. Casciotti, Technical updates to the bacterial method for nitrate isotopic analyses. *Analytical Chemistry* **83**, 1850-1856 (2011).
32. F. Gazeau *et al.*, Impact of dust addition on the metabolism of Mediterranean plankton communities and carbon export under present and future conditions of pH and temperature. *Biogeosciences* **18**, 5423-5446 (2021).
33. M. Caffin *et al.*, N2 fixation as a dominant new N source in the western tropical South Pacific Ocean (OUTPACE cruise). *Biogeosciences* **15**, 2565-2585 (2018).
34. R. Alkalay *et al.*, Carbon export and drivers in the southeastern Levantine Basin. *Deep-Sea Research Part Ii-Topical Studies in Oceanography* **171**, (2020).
35. E. Ternon *et al.*, The impact of Saharan dust on the particulate export in the water column of the North Western Mediterranean Sea. *Biogeosciences* **7**, 809-826 (2010).

36. D. M. Karl *et al.*, in *Ocean Biogeochemistry: The Role of the Ocean Carbon Cycle in Global Change,* Fasham, Ed. (Springer, New York, 2003), pp. 239-267.
37. M. W. Lomas, N. R. Bates, R. J. Johnson, D. K. Steinberg, T. Tanioka, Adaptive carbon export response to warming in the Sargasso Sea. *Nature Communications* **13**, 1211 (2022).
38. D. M. Karl *et al.*, Seasonal-to-decadal scale variability in primary production and particulate matter export at Station ALOHA. *Progress in Oceanography* **195**, (2021).

Submitted Manuscript: Confidential
April 2022

Natural iron fertilization by shallow hydrothermal sources fuels diazotroph blooms in the Ocean

Authors: Sophie Bonnet[1], Cécile Guieu[2], Vincent Taillandier[2], Cédric Boulart[3], Pascale Bouruet-Aubertot[4], Frédéric Gazeau[2], Carla Scalabrin[5], Matthieu Bressac[2], Angela N. Knapp[6], Yannis Cuypers[4], David González-Santana[7,8], Heather J. Forrer[6], Jean-Michel Grisoni[9], Olivier Grosso[1], Jérémie Habasque[7], Mercedes Jardin-Camps[1], Nathalie Leblond[2], Frédéric Le Moigne[1,7], Anne Lebourges-Dhaussy[7], Caroline Lory[1], Sandra Nunige[1], Elvira Pulido-Villena[1], Andrea L. Rizzo[10], Géraldine Sarthou[7], Chloé Tilliette[2]

Affiliations:
[1]Aix Marseille University, Université de Toulon, CNRS, IRD, MIO UM 110, 13288 Marseille, France
[2]Laboratoire d'Océanographie de Villefranche, Institut de la Mer de Villefranche, CNRS, Sorbonne Université, 06230 Villefranche-sur-Mer, France
[3]Adaptation et Diversité en Milieu Marin, UMR 7144 AD2M CNRS-Sorbonne Université, Station Biologique de Roscoff, 29680 Roscoff, France
[4]Laboratoire d'Océanographie et du Climat: Expérimentation et Approches Numériques (LOCEAN-IPSL), Sorbonne University, CNRS-IRD-MNHN, 75005 Paris, France
[5]Ifremer, Univ Brest, CNRS, UMR 6538 Geo-Ocean, F-29280 Plouzané, France
[6]Florida State University, Department of Earth, Ocean, and Atmospheric Sciences, Tallahassee, Florida, 32306, USA
[7]CNRS, Univ Brest, IRD, Ifremer, UMR 6539, LEMAR, Plouzane, France
[8]Instituto de Oceanografía y Cambio Global, IOCAG, Universidad de Las Palmas de Gran Canaria, 35017
[9]Institut de la Mer de Villefranche, IMEV, Sorbonne Université, Villefranche sur Mer
[10]Istituto Nazionale di Geofisica e Vulcanologia, Sezione di Palermo, Via Ugo La Malfa 153, 90146 Palermo, Italy

***Correspondence to:** sophie.bonnet@mio.osupytheas.fr, cecile.guieu@imev-mer.fr

Supprimé: [11]

Supprimé: [11]Istituto Nazionale di Geofisica e Vulcanologia, Sezione di Milano, Via Alfonso Corti 12, 20133 Milano, Italy

Code de champ modifié

Code de champ modifié

Abstract. Iron is an essential nutrient, regulating productivity in ~30% of the ocean. Compared to deep (>2000 m) hydrothermal activity at mid-ocean ridges that provide iron to the ocean's interior, shallow (<500 m) hydrothermal fluids are likely to influence the surface's ecosystem. However, their effect is unknown. Here we show that fluids emitted along the Tonga volcanic arc (South Pacific) have a dramatic impact on iron concentrations in the photic layer through vertical diffusion. This enrichment stimulates biological activity, resulting in an extensive patch of chlorophyll. Diazotroph activity is 2-8 times higher, and carbon export fluxes 2-3 times, compared to adjacent unfertilized waters. Such findings reveal a novel mechanism of natural iron fertilization in the ocean, fueling regional hot spot sinks for atmospheric CO_2.

One-Sentence Summary: Shallow hydrothermal iron fertilizes the overlying surface ocean creating an oasis in the desert

Supprimé: A

Planktonic diazotrophs are microscopic organisms ubiquitous in the ocean, that play a crucial role: they supply new available nitrogen (N) to the surface ocean biosphere, an essential but scarce nutrient in most of our oceans *(1, 2)*. Diazotrophs do so by converting atmospheric N_2 (endlessly available but metabolically useless) to ammonia (readily bioavailable), a reaction termed biological N_2 fixation. Diazotrophs thus alleviate N limitation in 60% of our oceans, especially in low latitudes, promoting CO_2 fixation by phytoplankton into organic carbon (primary productivity), that in turn, sustains the food web and organic carbon export and sequestration to the deep ocean (*3-6*). However, diazotrophs face a major challenge: besides phosphorus requirements, the iron (Fe)-rich nitrogenase enzyme that catalyzes N_2 fixation imposes a high Fe demand on diazotroph growth *(7)*, however Fe bioavailability in the ocean often limits the growth of these organisms *(6, 8)*. The Western subtropical South Pacific (WTSP) is a recognized hotspot of N_2 fixation activity, with an estimated contribution of ~21% to the global fixed N input *(9)*. Fe supply through atmospheric deposition is known to control large-scale diazotroph biogeography *(10)*, but such aeolian inputs are extremely low in this remote region *(11)*, suggesting the presence of alternative Fe fertilization processes underlying the ecological success of diazotrophs. Identifying these processes is of the utmost importance as diazotrophs have recently been identified as key drivers of future marine net primary productivity in response to climate change *(12)*. Here we demonstrate that Fe-rich fluids emitted by shallow hydrothermal venting directly fertilize the overlying surface ecosystem, inducing intense diazotroph activity supporting enhanced carbon export fluxes, with a C sequestration efficiency higher than those from artificial mesoscale Fe-addition experiments.

The WTSP hosts the Tonga-Kermadec subduction zone, stretching 2,500 km from New Zealand to Tonga (Fig. 1A). It is the fastest converging, most seismically active subduction zone, with the highest density of underwater volcanic centers on Earth *(13)*. This system produces extensive plumes of ^3He in the bathypelagic ocean (1500-2000 m) that fingerprint deep hydrothermal sources originating in the Lau basin *(14, 15)*. Other authors *(16, 17)* also identified shallower sources (<500 m) along the Tonga arc, associated with significantly elevated dissolved Fe (DFe) and manganese (DMn) concentrations close to the seafloor. Guieu et al. *(11)* demonstrated that these shallow sources were able to bring DFe up to the photic layer (~100 m) at high concentrations (up to 66 nmol liter^{-1}). These Fe infusions are hypothesized to fuel the observed N_2 fixation hot spot associated with an elevated chlorophyll (Chl) patch persisting 6 months per year in this region *(9, 11)* (Fig 2A,B). Yet, there is currently no empirical evidence of the direct effect of such hydrothermal Fe fertilization on the overlying planktonic ecosystem, with the implication that a significant part of new N entering the tropical Pacific -thanks to hydrothermal Fe- is likely missing from N budgets. Such an Fe supply mechanism would challenge the prevailing paradigm that diazotroph productivity is mainly mediated by Fe from dust deposition *(10)* in N-limited regions.

To document the mechanistic link between Fe supply from submarine volcanism and the response of the surface plankton community, we combine acoustic, chemical, physical, and biological data acquired during the GEOTRACES GPpr14 TONGA expedition *(18)*, a zonal transect between the Tonga volcanic arc and the South Pacific Gyre, which serves as a reference deep-sea site where the ocean surface is not impacted by hydrothermal activity. The targeted submarine volcano (Volcano #1 *(16, 17)*) is a large stratovolcano (basal diameter 28 km) located in the central part of the Tonga arc (-21.154 ; -175.744) (Fig. 1A, B). During an acoustic survey above the volcano, we detected multiple acoustic plumes (Fig. 1B, Table S1) rising from the sea floor up to ~20 m below the surface ocean (Fig. 1C). We focused our study on a site located near the caldera on the southwestern edge of the volcano (Fig. 1B) (hereafter referred

Supprimé: Atmospheric dinitrogen (N_2) fixed by diazotrophs provides the largest external source of new N to the surface ocean, supporting food webs and organic matter export in 60% of our oceans (*2, 6*).
Mis en forme : Anglais (E.U.)
Mis en forme : Anglais (E.U.)
Mis en forme : Anglais (E.U.)
Mis en forme : Anglais (E.U.)
Mis en forme : Anglais (E.U.)
Mis en forme : Anglais (E.U.)
Mis en forme : Anglais (E.U.)
Mis en forme : Anglais (E.U.)
Mis en forme : Anglais (E.U.)
Supprimé: but
Supprimé: its
Supprimé: mechanisms
Mis en forme : Français
Supprimé: ¶
Supprimé: seafloor of the
Supprimé: ese
Supprimé: s
Supprimé: are associated with
Supprimé: desert
Supprimé: ¶
Supprimé: ¶
Here,we combine acoustic, chemical, physical, and biological data acquired during the GEOTRACES GPpr14 TONGA expedition *(18)*
Supprimé: t
Supprimé: . We bring together multiple observations from
Supprimé: A
Supprimé: We demonstrate that Fe-rich fluids emitted by shallow hydrothermal venting directly fertilize the overlying surface ecosystem, inducing enhanced biological biomass and carbon export fluxes mostly due to the activity of N_2 fixing microbes.¶
¶
Supprimé: A
Supprimé: decided to

to as 'Panamax site'), where the acoustic anomaly *(19-21)*, also associated with intense gas bubble emissions, was strong and continuous (Fig. 1D). Repeated CTD casts at this site revealed that acoustic plumes were also associated with strong anomalies in pH, turbidity, and redox potential (Eh) (Fig. 1E, Table S2) from the seafloor (195 m depth) up to ~160 m. Methane concentrations that reached >100 nmol liter^{-1} (Fig. 1F) and the excess of ^{3}He and ^{4}He concentrations (Fig. S1) confirmed the hydrothermal origin of the plumes.

DFe and DMn were also enriched ~80-fold at this site (Fig. 1F) compared to similar depths in the WTSP *(11, 22)*. DFe and CH_4 concentrations were positively correlated (R^2=0.89, p<0.05). DFe reached concentrations as high as 48.5 nmol liter^{-1} at 195 m (within the main acoustic signal), and although they decreased towards the photic layer (~0-100 m), DFe concentrations in that layer (~0.6 to 10 nmol liter^{-1}) (Fig. 1F) were one order of magnitude higher compared to those at stations not impacted by hydrothermal activity *(23)*. The turbulence profiles (Fig. S2) revealed an order of magnitude higher vertical diffusivity above the volcano (Kz = 3.7±1.9x10^{-5} m^2 s^{-1} at ~50 m, corresponding to the base of the surface mixed layer) compared to the distal open-sea reference site (Kz = 5.2±9.6x10^{-6} m^2 s^{-1}) (Table 1), in line with previous work above shallow (~200 m) seamounts (*24*). Combining the measured Kz with the DFe gradients (Table 1 and Supplementary materials), the diffusive DFe vertical supply to the mixed layer above the volcano reached 1.1±1.7x10^{-4} mmol Fe m^{-2} d^{-1}. This is orders of magnitude larger than at the reference site (Table 1), suggesting that Fe-rich fluids released close to the shallow volcano represent a significant Fe source to surface waters. A phosphate supply of 5.4±2.4x10^{-3} mmol m^{-2} d^{-1} accompanied this vertical DFe supply, while no nitrate supply could be quantified (Table S4) due to the decoupling between the depth of the phosphacline (~50 m) and the nitracline (~100 m) (Fig. S5), as already observed in the WTSP (*25*).

Along the west to east zonal transect, total chlorophyll-a (Chl*a)* and particulate organic N stocks peaked in the naturally Fe-fertilized waters at Volcano #1 (Fig. 2). Both were also elevated up and downstream of the arc (Fig. 2C) consistent with ocean color images (Fig. 2A). This biomass peak was associated with 2 to 8-fold enhanced N_2 fixation rates relative to surrounding waters on either side of the arc (p<0.05, Mann-Whitney test) (Fig 2E), and 90-fold higher *Trichodesmium* spp. abundances (p<0.05, Mann-Whitney test) (Fig. 2F). This led to extremely high N_2 fixation rates and *Trichodesmium* spp. abundances in the Fe-fertilized waters (>2000 µmol N m^{-2} d^{-1} ; ~6 x 10^7 *nifH* copies L^{-1}), i.e. one to two orders of magnitude greater than values commonly found in other (sub)tropical ocean basins (*26*). This peak in diazotroph activity was marked by a phosphate drawdown (~50 nM) in the photic layer, although concentrations were not limiting for *Trichodesmium* spp. *(27)* due to intense microbial phosphorus cycling in this region *(28)*. Diazotrophs were favored by the extremely low nitrate concentrations along the transect (Fig. S6).

The particulate organic carbon (POC) and nitrogen (PON) export fluxes were measured using surface tethered sediment traps deployed for 4 days near Volcano #1 and at the reference site. Consistent with model simulations in this region *(22)*, POC export at 170 m and 270 m was 2 to 3 times higher in the Fe-fertilized patch than at the reference site (Table 1), resulting in an excess of POC export of 1.5 to 2.5 mmol C m^{-2} d^{-1} in the fertilized waters. Comparing measurements of subsurface water column nitrate+nitrite δ^{15}N (1.2 to 2.2‰) with the δ^{15}N of sinking PON (-0.5± 3.5‰ at 170 m and -0.2± 1.9‰ at 270 m, respectively), the N isotope budget (N_2 fixation end member = -1‰) revealed that N_2 fixation supported 77 to 84±159% at 170 m and 64 to 75±86% at 270 m of the export production in the Fe-fertilized area, consistent with the massive export of diazotrophs observed in the traps during the expedition *(3, 29)*. Collectively, these results suggest that the hydrothermally-driven Fe fertilization fuels

Supprimé: together

Supprimé: repeated

Supprimé: nitrogen

Supprimé: a

Supprimé: adjacent

Supprimé: to

Supprimé: A

Supprimé: . The

Mis en forme : Indice

Supprimé: N_2 fixation

Supprimé: of >2000 µmol N m^{-2} d^{-1}

Mis en forme : Non Exposant/ Indice

Supprimé: were associated with ~90-fold higher *Trichodesmium* spp. abundances (~6 x 10^7 *nifH* copies L^{-1}) compared to abundances observed on either side of the Arc (p<0.05, Mann-Whitney test) (Fig. 2F) and

Supprimé: a

planktonic diazotrophs, resulting in low $\delta^{15}N$ of sinking PON and high POC export fluxes compared to subtropical systems not impacted by hydrothermal activity *(30)* (Table S5).

To confirm the causal link between hydrothermal inputs and diazotroph activity, we conducted novel experiments where hydrothermally-enriched waters collected at the 'Panamax site' of Volcano #1 (hereafter referred to as 'plume water') were supplied to surface biological communities using 300-L trace metal clean reactors (Fig. S7A, Methods). Increasing plume water volumes (from 0 to 14.5% of the total reactors volume) were added to surface seawater from outside of the direct volcanic influence (-21.683°N ; -174.709°E). The plume water was characterized by low pH (6.4) compared to ambient seawater (8.1) and DFe concentrations (15.8 nmol liter^{-1}) were ~15-fold higher than in ambient surface waters (1.0 nmol liter^{-1}) (Table S6). The increasing additions resulted in consistent increases of DFe concentrations and decreasing pH in the experimental reactors (Fig. S7). Plume water additions enhanced N_2 fixation rates by a factor of 7 to 8 on average over all sampling days compared to those measured in the unamended control ($p<0.05$, Mann-Whitney test) (Fig. 3A), reaching levels in the same range as *in situ* rates measured above the volcano (Fig. 2E). Likewise, as observed *in-situ*, *Trichodesmium* abundances increased by a factor of 3 to 5-fold ($p<0.05$, Mann-Whitney test) in plume water-amended reactors (Fig. 3B). Both N_2 fixation rates and *Trichodesmium* abundances decreased at the end of the experiment, likely as a consequence of phosphate depletion in the closed reactors (no possible turbulent diffusion) (Fig. S7), but generally remained higher in the amended reactors compared to those measured in the control. Due to the low inorganic N:P molar ratio (~9:1) in the plume water (indicative of a greater phosphate availability relative to nitrate), the mixing of the plume water with surface seawater likely prevented the phosphate limitation for up to days 6-8, while nitrate was depleted after 2 days. This decoupling between nitrate and phosphate also mirrors the *in situ* data described above.

The Fe supply from the Tonga arc thus drives in large part upper ocean phenology of biological activity. We estimate that the region of elevated Chl*a* extends ~800 km in longitude and ~450 km in latitude (Fig. 1A), forming a hot spot of biological activity of ~360,000 km^2 in the middle of the otherwise desert-like WTSP. The trajectories of SVP (surface velocity program) drifters deployed above Volcano #1 indicate that over a 6-month period, Fe-fertilized water masses can be dispersed regionally and support this extended Chl*a* patch (Fig. S8). The trajectories provide a bulk representation of complex dynamical processes occurring at smaller scales, involving the South Equatorial current and modulated by mesoscale activity *(11, 31)*, or lateral stirring by filaments *(32)*. In addition, multiple active vent fields have been (recently) identified along the Tonga arc and the Lau Basin *(16, 17, 33, 34)*, either at shallow depths (<500 m) or deeper (500-1000 m). Although all active shallow vents have not yet been discovered, with a density estimation of one active volcano center per 12 km of arc, fertilization processes such as those evidenced at Volcano #1 likely occur at many locations along the arc, further explaining the regional extent of the Chl*a* patch observed by satellite (Fig. 2A). We cannot exclude that the few emerged Tonga islands could provide additional nutrients, likely contributing to the observed bloom. However, a study conducted over the entire tropical Pacific reveals that these island mass effects are generally very localized (around the islands, with a Chl*a* patch area of 9-13 km^2) and are of moderate amplitude (+9% of Chl*a* increase relative to background waters) *(35)*. In contrast, the bloom in the region of the Tonga volcanic arc is unique in that it is much larger (360,000 km^2) and of greater amplitude (~100% Chl*a* increase) than around any other Pacific islands/archipelagos. This means that additional Fe sources of hydrothermal origin are necessary to sustain such a bloom. As an example, very weak Chl*a* is observed around the Cook Islands located at the same latitude as Tonga, receiving the same amount of rainfall and aerosol-Fe deposition annually, but not impacted by hydrothermal activity (Fig. S9), confirming that

Supprimé: enhanced POC export and
Mis en forme : Police :Non Italique
Mis en forme : Police :Non Italique
Supprimé: hydrothermal fluid
Supprimé: fluid
Supprimé: hydrothermal fluid
Supprimé: 5
Supprimé: Fluid
Supprimé: fluid
Supprimé: hydrothermal
Supprimé: fluid
Supprimé: fluid
Supprimé: A
Supprimé: such an
Supprimé: A
Supprimé: A
Supprimé: A
Supprimé: fuel locally
Supprimé: precipitations
Supprimé: annually

nutrients of terrestrial origin are not sufficient to sustain blooms of large amplitude. Finally, some extremely rare events such as the massive eruption of the Hunga Tonga Hunga Ha'apai volcano in January 2022 could also cause short-term localized blooms, such as the one observed from satellite following the eruption *(36)*, that had no visible effect on the interannual trend of Chl*a*. Other authors suggest that the interpretation of the Chl*a* increase after the eruption was distorted by the presence of abundant volcanic particles suspended in the water column following the eruption *(37)*.

Looking more deeply into the 25-year monthly Chl*a* time series (Fig. 2B, S10), we find that, despite interannual variability, the bloom develops every year for at least 6 months in austral summer. This seasonal characteristic is probably linked to the thermal fitness of *Trichodesmium,* who are thought to only bloom at temperatures >25°C -reached in the WTSP between November and April (austral summer)-. This thermal constraint for *Trichodesmium* also probably explains why the bloom does not extend south of ~23°S, which marks the location of the 25°C isotherm. Further south, surface waters are also depleted in nitrate, and in the absence of diazotrophs, the new Fe supplied by hydrothermal vents along the arc cannot be taken up to produce new biomass. As models predict a sea surface temperature increase of 1.5°C by the end of the century in the Tonga arc region (*38*), it is possible that the thermal constraint for diazotrophs will be relieved and the bloom will spread further south in the future.

To properly account for the seasonal variability of export, we deployed a moored sediment trap at 1000 m for a full annual cycle in the fertilized patch (see SI). We show that POC export was 5 times higher in austral summer compared to winter (Fig. 4), resulting in a seasonally-integrated (6 summer months) POC export of 74 mmol C m^{-2}, i.e. 80% of the annual POC export flux. The low $\delta^{15}N$ signature of sinking PON during these summer months (~0-1‰) confirms that N_2 fixation supports most export production during that season. In austral winter, the higher sinking PON $\delta^{15}N$ values (2-8‰) suggest that other N sources (i.e., deep nitrate) fuel the low export production. For comparison, the annual POC flux measured here in the subtropical ocean is of the same order of magnitude as that measured in the Southern Ocean in naturally Fe-fertilized waters (*39, 40*). This suggests that Fe-fertilized regions of the oligotrophic ocean can act as net CO_2 sinks, provided sufficient phosphorus availability. The Fe-fertilized WTSP is a unique ecosystem allowing C sequestration supported by N_2 fixation due to substantial winter phosphate replenishment (not associated with nitrate supply due to decoupling of phosphacline and nitracline depths) (*25*) and to a turbulent diffusive flux of Fe and phosphate (19 mmol : mol^{-1}) meeting *Trichodesmium* requirements (*41*). Furthermore, *Trichodesmium* can reduce its P quotas under P stress (*42, 43*), and actively utilizes dissolved organic P (DOP) compounds in this region (*44*), likely enhanced by high Fe availability (*45*). Taken together, this suggests that P and Fe work in concert to trigger extensive diazotroph blooms and C sequestration by N_2-based new production in the WTSP.

Compared to shelf-driven natural Fe fertilizations occurring in HNLC (High Nutrient, Low Chlorophyll) waters of the Southern Ocean (SO), the TONGA bloom is generally more temporally and spatially extensive, despite its lower intensity (depth integrated Chl*a*) (Table 1) *(39, 46-48)*. The total DFe flux in this study (130 nmol Fe m^{-2} d^{-1}) was generally lower than that measured in Fe-enriched waters downstream of the Kerguelen plateau (KEOPS cruise in 2005, 222 nmol Fe m^{-2} d^{-1} *(49)*) and downstream of the Crozet plateau (CROZEX cruise in 2004, 550 nmol Fe m^{-2} d^{-1} *(39)*) (Table 1). However, unlike HNLC regions, surface waters of the WTSP are nitrate-depleted, and only N_2-fixing organisms can exploit this new Fe to build biomass and drive carbon export to the deep ocean, as long as sufficient phosphorus remains available. Based on the excess POC export and the excess of DFe supply at the time of the cruise (Table 1), we calculated a C sequestration efficiency (defined as the ratio of the excess

Supprimé: explosion
Supprimé: explosion
Supprimé: explosion
Supprimé: explosion
Supprimé: S
Supprimé: make
Supprimé: at
Mis en forme : Indice
Supprimé: (*40*)
Supprimé: ¶
Mis en forme : Police :Non Italique
Mis en forme : Police :Non Italique
Mis en forme : Police :Non Italique
Mis en forme : Police :Non Italique
Mis en forme : Police :Non Italique
Mis en forme : Police :Non Italique
Mis en forme : Police :Non Italique
Mis en forme : Police :Non Italique
Supprimé: (*25*)(*41, 42*)(*43*)
Supprimé: longer and larger

POC export to the amount of excess DFe supplied) of 13600 and 23000 mol C mol^{-1} Fe (at 170 and 270 m, respectively). Although comparisons between studies need to be considered with caution given the different methods used and timescales considered to estimate both excess Fe supply and POC export, this sequestration efficiency is higher than those from artificial mesoscale Fe-addition experiments (e.g. 4300 mol mol^{-1} for SOFeX *(50)*; 1200 mol mol^{-1} for SERIES *(51)*), and in the range of values measured in naturally-fertilized HNLC regions (8600 mol mol^{-1} for CROZEX *(39)* to 154,000 mol mol^{-1} during KEOPS *(49)*). This confirms that natural Fe fertilizations are more efficient for carbon sequestration than purposeful Fe additions. In addition, comparing such estimates from various natural oceanic settings, Le Moigne et al. *(52)* suggested that the apparent variability in C sequestration efficiency may be related to the timescale of Fe delivery (slow delivery being more efficient). Therefore, attention must be paid in future studies to the timescale of delivery of this newly-recognized mode of Fe supply through shallow hydrothermalism, including in temperate and polar ecosystems, where this efficiency could be even more important due to higher macronutrient availability.

Our conceptual view of the ocean Fe cycle has greatly evolved over the past 10 years, highlighting the importance of hydrothermal activity on the Fe cycle *(53)*. While model simulations suggest that hydrothermal inputs associated with mid-ocean ridges (>2000 m) contribute 23% of the Fe found in the global ocean water column, that Fe only directly supports 3% of carbon export at 100 m *(54)*. This is mostly because a large part of that Fe remains in the deep ocean over long time scales *(53)* and needs to be entrained in surface waters before potentially impacting photosynthetic communities *(46, 48)*. Fe from intermediate depth (~1000 m) vents may also be transported long distances and with the condition that these waters upwell, influence marine ecosystems located thousands of km far from the site of discharge *(55)*. However, hydrothermal venting also occurs at shallower depths (<500 m) in island arc systems such as the Tonga arc. Even if scavenging and precipitation removes part of this newly-emitted Fe from the dissolved pool *(23)*, such shallow sources can supply Fe rapidly to overlying surface photosynthetic communities compared to Fe emitted deeper *(23, 55)*. In the oligotrophic ocean, the implications of such shallow hydrothermal Fe fertilization are highly significant as they directly fuel surface diazotrophs and export of organic matter to the deep ocean, representing regional hotspot sinks of atmospheric CO_2. We demonstrate here that shallow hydrothermal sources also represent a triggering factor on diazotroph blooms in regions where the atmospheric supply of DFe is virtually absent. Such forcing is of the utmost importance to study as climate models predict an expansion of the oligotrophic gyres (40% of our oceans) *(56)* where diazotrophs will likely thrive. Furthermore, in a warmer, more stratified ocean, such shallow Fe sources are likely to deliver Fe to surface communities more readily than deep sources *(55)*. Beyond the oligotrophic oceans, shallow hydrothermal fertilizations are likely to be common in the global ocean, due to the high number of shallow hydrothermal vents associated with island arc systems and submarine volcanic calderas (*57*) whose exact number/locations are still yet to be discovered *(14)*. Such systems are also present at higher latitudes, notably in the HNLC waters in the subarctic Pacific and the SO *(57)*. Therefore, a comprehensive evaluation of their impact in these severely Fe-limited systems where surface mixed layers reach the intermediate or even the deep ocean/ water masses is clearly needed. Finally, the extent to which such hydrothermal-driven biological carbon pump enhancement may have changed atmospheric CO_2 in the past remains unclear. Future studies would be relevant as the hydrothermal flux of Fe has been relatively constant over millennial timescales *(58)*.

Supprimé: Yet, model simulations suggest that, although hydrothermal inputs associated with mid-ocean ridges (>2000 m) contribute to a significant part of the water column Fe inventory (23% of the ocean's total), they only directly support 3% of carbon export at 100 m

Supprimé: o

Supprimé: A

Supprimé: ism

References and Notes

1. C. M. Moore *et al.*, Processes and patterns of oceanic nutrient limitation. *Nature Geoscience* **6**, 701–710 (2013).
2. N. Gruber, in *Nitrogen in the marine environment*. (2008), pp. 1-50.
3. S. Bonnet *et al.*, Diazotrophs are overlooked contributors to carbon and nitrogen export to the deep ocean. *The ISME journal* **17**, 47-58 (2022).
4. D. M. Karl, M. J. Church, J. E. Dore, R. Letelier, C. Mahaffey, Predictable and efficient carbon sequestration in the North Pacific Ocean supported by symbiotic nitrogen fixation. *Proceedings of the National Academy of Sciences* **109**, 1842–1849 (2012).
5. A. Subramaniam *et al.*, Amazon River enhances diazotrophy and carbon sequestration in the tropical North Atlantic Ocean. *Proceedings of the National Academy of Sciences* **105**, 10460–10465 (2008).
6. J. P. Zehr, D. G. Capone, Changing perspectives in marine nitrogen fixation. *Science* **368**, (2020).
7. C. Lory *et al.*, Assessing the contribution of diazotrophs to microbial Fe uptake using a group specific approach in the Western Tropical South Pacific Ocean. *ISME Communications* **2**, 1-11 (2022).
8. J. A. Sohm, E. A. Webb, D. G. Capone, Emerging patterns of marine nitrogen fixation. *Nature Reviews Microbiology* **9**, 499-508 (2011).
9. S. Bonnet, M. Caffin, H. Berthelot, T. Moutin, Hot spot of N2 fixation in the western tropical South Pacific pleads for a spatial decoupling between N2 fixation and denitrification. *Proceedings of the National Academy of Sciences* **114**, E2800-E2801 (2017).
10. C. Schlosser *et al.*, Seasonal ITCZ migration dynamically controls the location of the (sub)tropical Atlantic biogeochemical divide. *Proceedings of the National Academy of Sciences of the United States of America* **111**, 1438-1442 (2014).
11. C. Guieu *et al.*, Iron from a submarine source impacts the productive layer of the Western Tropical South Pacific (WTSP). *Scientific Reports* **8**, 9075 (2018).
12. L. Bopp *et al.*, Diazotrophy as a key driver of the response of marine net primary productivity to climate change. *Biogeosciences* **19**, 4267-4285 (2022).
13. C. E. J. de Ronde *et al.*, in *Volcanic, Geothermal, and Ore-Forming Fluids: Rulers and Witnesses of Processes within the Earth*. (Society of Economic Geologists, 2005), vol. 10, pp. 0.
14. C. R. German *et al.*, Hydrothermal impacts on trace element and isotope ocean biogeochemistry. *Phil. Trans. R. Soc. A* **374**, 20160035 (2016).
15. J. E. Lupton, D. G. Pyle, W. J. Jenkins, R. Greene, L. Evans, Evidence for an extensive hydrothermal plume in the Tonga-Fiji region of the South Pacific. *Geochem Geophy Geosy* **5**, (2004).
16. P. Stoffers *et al.*, Submarine volcanoes and high-temperature hydrothermal venting on the Tonga arc, southwest Pacific. *Geology* **34**, 453-456 (2006).
17. G. Massoth *et al.*, Multiple hydrothermal sources along the south Tonga arc and Valu Fa Ridge. *Geochemistry, Geophysics, Geosystems* **8**, (2007).
18. C. Guieu, S. Bonnet, TONGA GEOTRACES GPpr14 ocean expedition, https://doi.org/10.17600/18000884. (2019).
19. C. Boulart *et al.*, Active hydrothermal vents in the Woodlark Basin may act as dispersing centres for hydrothermal fauna. *Commun Earth Environ* **3**, (2022).
20. W. W. Chadwick *et al.*, Imaging of CO2 bubble plumes above an erupting submarine volcano, NW Rota-1, Mariana Arc. *Geochem Geophy Geosy* **15**, 4325-4342 (2014).
21. N. Feuillet *et al.*, Birth of a large volcanic edifice offshore Mayotte via lithosphere-scale dyke intrusion. *Nature Geoscience* **14**, 787-+ (2021).

22. J. A. Resing *et al.*, Basin-scale transport of hydrothermal dissolved metals across the South Pacific Ocean. *Nature* **523**, 200-203 (2015).
23. C. Tilliette *et al.*, Dissolved Iron Patterns Impacted by Shallow Hydrothermal Sources Along a Transect Through the Tonga-Kermadec Arc. *Global Biogeochemical Cycles* **36**, e2022GB007363 (2022).
24. J. Lavelle, I. Lozovatsky, D. Smith IV, Tidally induced turbulent mixing at Irving Seamount—modeling and measurements. *Geophysical research letters* **31**, (2004).
25. T. Moutin *et al.*, Nutrient availability and the ultimate control of the biological carbon pump in the western tropical South Pacific Ocean. *Biogeosciences* **15**, 2961-2989 (2018).
26. Y.-W. Luo *et al.*, Database of diazotrophs in global ocean: abundance, biomass and nitrogen fixation rates. *Earth System Science Data* **4**, 47-73 (2012).
27. A. Filella *et al.*, Contrasting Roles of DOP as a Source of Phosphorus and Energy for Marine Diazotrophs. *Frontiers in Marine Science* **9**, (2022).
28. F. Van Wambeke *et al.*, Dynamics and controls of heterotrophic prokaryotic production in the western tropical South Pacific Ocean: links with diazotrophic and photosynthetic activity. *Biogeosciences* **15**, 2669-2689 (2018).
29. M. Benavides *et al.*, Sinking Trichodesmium fixes nitrogen in the dark ocean. *The ISME journal* **16**, 2398-2405 (2022).
30. A. N. Knapp *et al.*, Distribution and rates of nitrogen fixation in the western tropical South Pacific Ocean constrained by nitrogen isotope budgets. *Biogeosciences* **15**, 2619-2628 (2018).
31. L. Rousselet *et al.*, Large- to submesoscale surface circulation and its implications on biogeochemical/biological horizontal distributions during the OUTPACE cruise (southwest Pacific). *Biogeosciences* **15**, 2411-2431 (2018).
32. A. de Verneil, L. Rousselet, A. M. Doglioli, A. A. Petrenko, T. Moutin, The fate of a southwest Pacific bloom: gauging the impact of submesoscale vs. mesoscale circulation on biological gradients in the subtropics. *Biogeosciences* **14**, 3471-3486 (2017).
33. S. E. Beaulieu, E. T. Baker, C. R. German, A. Maffei, An authoritative global database for active submarine hydrothermal vent fields. *Geochem Geophy Geosy* **14**, 4892-4905 (2013).
34. C. R. German *et al.*, Hydrothermal impacts on trace element and isotope ocean biogeochemistry. *Philosophical Transactions of the Royal Society A: Mathematical, Physical and Engineering Sciences* **374**, (2016).
35. M. Messie, A. Petrenko, A. M. Doglioli, E. Martinez, S. Alvain, Basin-scale biogeochemical and ecological impacts of islands in the tropical Pacific Ocean. *Nature Geoscience* **15**, 469-+ (2022).
36. B. Barone, R. M. Letelier, K. H. Rubin, D. M. Karl, Satellite Detection of a Massive Phytoplankton Bloom Following the 2022 Submarine Eruption of the Hunga Tonga-Hunga Ha‘apai Volcano. *Geophysical Research Letters* **49**, e2022GL099293 (2022).
37. A. Whiteside *et al.*, Impact of ashes from the 2022 Tonga volcanic eruption on satellite ocean color signatures. *Frontiers in Marine Science* **9**, (2023).
38. L. Dhage, M. J. Widlansky, Assessment of 21st Century Changing Sea Surface Temperature, Rainfall, and Sea Surface Height Patterns in the Tropical Pacific Islands Using CMIP6 Greenhouse Warming Projections. *Earths Future* **10**, (2022).
39. R. T. Pollard *et al.*, Southern Ocean deep-water carbon export enhanced by natural iron fertilization. *Nature* **457**, 577-580 (2009).
40. M. Rembauville, I. Salter, N. Leblond, A. Gueneugues, S. Blain, Export fluxes in a naturally iron-fertilized area of the Southern Ocean - Part 1: Seasonal dynamics of

particulate organic carbon export from a moored sediment trap. *Biogeosciences* **12**, 3153-3170 (2015).
41. J. Nuester, S. Vogt, M. Newville, A. B. Kustka, B. S. Twining, The unique biogeochemical signature of the marine diazotroph trichodesmium. *Frontiers in microbiology* **3**, 150 (2012).
42. D. M. Karl, R. Letelier, D. V. Hebel, D. F. Bird, C. D. Winn, *Trichodesmium blooms and new nitrogen in the North Pacific Gyre*. C. D. G. R. J. G. Carpenter E.J., Ed., Marine pelagic cyanobacteria:Trichodesmiurn and other diazotrophs. (Kluwer Academic Publishers, Dordrecht, 1992), pp. 219-237.
43. A. E. White, Y. H. Spitz, D. M. Karl, R. M. Letelier, Flexible elemental stoichiometry in Trichodesmium spp. and its ecological implications. *Limnology and Oceanography* **51**, 1777-1790 (2006).
44. Z. Liang, R. T. Letscher, A. N. Knapp, Dissolved organic phosphorus concentrations in the surface ocean controlled by both phosphate and iron stress. *Nature Geoscience* **15**, 651-+ (2022).
45. T. J. Browning *et al.*, Iron limitation of microbial phosphorus acquisition in the tropical North Atlantic. *Nature Communications* **8**, (2017).
46. M. Ardyna *et al.*, Hydrothermal vents trigger massive phytoplankton blooms in the Southern Ocean. *Nat Commun* **10**, 2451 (2019).
47. S. Blain, S. Bonnet, C. Guieu, Dissolved iron distribution in the tropical and sub tropical South Eastern Pacific. *Biogeosciences* **5**, 269–280 (2008).
48. C. M. S. Schine *et al.*, Massive Southern Ocean phytoplankton bloom fed by iron of possible hydrothermal origin. *Nat Commun* **12**, 1211 (2021).
49. S. Blain *et al.*, Effect of natural iron fertilization on carbon sequestration in the Southern Ocean. *Nature* **446**, 1070-1074 (2007).
50. K. O. Buesseler, J. E. Andrews, S. M. Pike, M. A. Charette, The effect of iron fertilization on carbon sequestration in the Southern ocean. *Science* **304**, 414-417 (2004).
51. P. W. Boyd *et al.*, The decline and fate of an iron-induced subarctic phytoplankton bloom. *Nature* **428**, 549-553 (2004).
52. F. A. C. Le Moigne *et al.*, Sequestration efficiency in the iron-limited North Atlantic: Implications for iron supply mode to fertilized blooms. *Geophysical Research Letters* **41**, 4619-4627 (2014).
53. A. Tagliabue *et al.*, The integral role of iron in ocean biogeochemistry. *Nature* **543**, 51-59 (2017).
54. A. Tagliabue, O. Aumont, L. Bopp, The impact of different external sources of iron on the global carbon cycle. *Geophysical Research Letters* **41**, 920-926 (2014).
55. W. Jenkins *et al.*, An intermediate-depth source of hydrothermal 3He and dissolved iron in the North Pacific. *Earth and Planetary Science Letters* **539**, 116223 (2020).
56. J. J. Polovina, E. A. Howell, M. Abecassis, Ocean's least productive waters are expanding. *Geophysical Research Letters* **35**, (2008).
57. J. A. Hawkes, D. P. Connelly, M. J. A. Rijkenberg, E. P. Achterberg, The importance of shallow hydrothermal island arc systems in ocean biogeochemistry. *Journal of Geophysical Research*, (2014).
58. N.-C. Chu *et al.*, Evidence for hydrothermal venting in Fe isotope compositions of the deep Pacific Ocean through time. *Earth and Planetary Science Letters* **245**, 202-217 (2006).

Acknowledgments: The dataset presented here resulted from the efforts of many individuals both onboard and on land who contributed to the success of the expedition. We thank the captain

and the crew of the R/V *L'Atalante* (TGIR Flotte, operated by IFREMER), in particular S. Laville Saint-Martin and J. Le Doare for their help during the multibeam survey, as well as the Technical Division INSU for the provision of the equipment. We thank the captain and the crew of the R/V *Alis* (TGIR Flotte, operated by IFREMER), for the safe recovery of the fixed mooring in particularly difficult weather conditions. We thank Céline Dimier and the SAPIGH platform of the Institut de la Mer de Villefranche (IMEV) for sampling on board and performing the pigment analyses. Finally, we thank Mr Lucas Jr for the English editing. Finally we are very grateful and thank JP Gattuso, S. Blain, A. Tagliabue and L. Guidi for their advice on the manuscript.

Funding:
Agence Nationale de Recherche grant ANR-18-CE01-0016 (SB, CG)
A-Midex grant TONGA (SB, CG)
Institut National des Sciences de l'Univers Les Enveloppes Fluides et l'Environnement grant TONGA (SB, CG)
TGIR Flotte océanographique française TONGA cruise (CG, SB)
MEMESTRA Grant (CB)
US NSF-OCE 1829797 (ANK)

Author contributions:
Conceptualization: SB, CG
Methodology: SB, CG, CB, FG
Investigation: SB, CG, VT, CB, FG, MB, DGS, JMG, OG, JH, CL, EP, GS, CT
Data curation: SB, CG, VT, CB, PBA, CS, FG, MB, ANK, YC, DGS, HJF, JH, NL, SN, ALR, GS, CS
Visualization: SB, CG, CB, FG, PBA, ANK, HJF
Writing – original draft: SB, CG
Writing – review & editing: All

Competing interests: Authors declare that they have no competing interests.
Data and materials availability: All data are available in the main text or the supplementary materials. The delta ^{15}N data are deposited to the BCO-DMO database https://www.bco-dmo.org/dataset/869963. The biogeochemical data are deposited on the INSU-LEFE-CYBER database http://www.obs-vlfr.fr/proof/php/TONGA/tonga_log_basicfiles.php and the acoustic data on the SEANOE database https://campagnes.flotteoceanographique.fr/campagnes/18000884/

Supplementary Materials
Materials and Methods
References (1-32)
Figs. S1 to S10
Tables S1 to S5

Figure legends.

Fig. 1. Acoustic, optical and chemical anomalies measured above Volcano #1. (A) Location map showing the Tonga volcanic arc system and Volcano #1 (V1, red triangle, -21.154; 175.744). (B) Bathymetry of Volcano #1 performed during TONGA, and position of the fluid/gas active sites detected by the multibeam echo sounder (EM710, 70-110 kHz) during the survey. The white circle represents the specific site studied here ('Panamax site'), from which the data are shown in panels C, D, E, F. (C) Multibeam echo sounder image (EM710, 70-110 kHz) showing hydrothermal gas and fluid emissions from the seafloor rising up to ~10 m below the sea surface. (D) Time series (11h) of acoustic signal detected by the sounder EK60 (38kHz) showing gas/fluid seafloor emissions at a fixed position (visualization threshold -75dB). (E) Vertical CTD profiles of temperature, pH, turbidity, and Eh in the main acoustic signal. (F) Vertical profiles of methane (CH_4, nM), dissolved Mn (nM), and dissolved Fe (nM) concentrations above Volcano #1.

Fig. 2. Chlorophyll patch in the vicinity of Tonga and associated biogeochemical and biological parameters. (A) Surface [Chl*a*] MODIS composite averaged over the time period corresponding to the TONGA cruise (1 November-6 December 2019) at a resolution of 4 km and zoom of the bloom region (~360 000 km^2). The bloom is delineated by the isoline 0.9 µg $liter^{-1}$ (corresponding to twice the average background [Chl*a*] concentration outside the bloom. (B) Monthly climatology of [Chl*a*] from a 25 years-time series (GLOBCOLOR product) at 2 sites along 20°S; the red line corresponds to the region of the Tonga bloom represented with the red dot on panel (A), and the blue line corresponds to the location of the reference site in the South Pacific Gyre, represented as a blue dot on panel (A). Horizontal and vertical distributions of (C) Total Chl*a* concentrations (µg L^{-1}), (D) Particulate organic nitrogen concentrations (µmol L^{-1}), (E) N_2 fixation rates (nmol N L^{-1} d^{-1}), (F) *Trichodesmium* abundances (Log nifH gene copies L^{-1}), (G) Dissolved Fe concentrations (nmol $liter^{-1}$). Y axis: depth (m), X axis: longitude; grey dots correspond to sampling depths at the various stations.

Fig. 3. Experimental evidence of the impact of hydrothermally-enriched water additions on diazotroph communities. Temporal evolution of (A) N_2 fixation rates (nmol N L^{-1} d^{-1}), (B) *Trichodesmium* abundances (*nifH* gene copies L^{-1}) along the 196h of the experiment in the control treatment (no fluid addition), and in the reactors amended with 1.8%, 5.5%, and 14.5% of 'plume water' collected at the 'Panamax site' of Volcano #1 (~200 m depth). Error bars correspond to standard deviations on triplicate analyses.

Fig. 4. Seasonal variability of export at 1000 m in the Fe-fertilized patch over one year (fixed mooring deployed at -20.702; -177.866 from Nov. 2019-Nov 2020; see SI)). Blue line: particulate organic carbon (POC) export fluxes (mmol C m^{-2} d^{-1}). Red line: δ15N (per mil) signature of exported PON.

Supprimé: hydrothermal

Supprimé: fluids

Table 1. Carbon and Fe budgets in the naturally-fertilized region of the Tonga volcanic arc and the distal reference site, and comparisons with natural fertilizations in HNLC regions.

	TONGA		CROZEX (2,5)	KEOPS (2
	+Fe (Volcano #1)	-Fe (Gyre)		
Bloom area (km^2)	360000	No bloom	90000	45000
Bloom duration (d)	180	-	58	75-105
Integrated Chla over the euphotic zone (mg Chl*a* m^{-2})	39	-	98.1	72-318
Vertical diffusivity (Kz, m^2 s^{-1})	$3.7 \pm 1.9 \times 10^{-5}$	$5.2 \pm 9.6 \times 10^{-6}$		
Vertical DFe gradient (mol m^{-4})	$3.1 \pm 4.7 \times 10^{-8}$	$7.8 \pm 3.1 \times 10^{-11}$		
Vertical DFe diffusive flux (mmol Fe m^{-2} d^{-1})	$1.1 \pm 1.7 \times 10^{-4}$	$3.5 \pm 3.1 \times 10^{-8}$	6.0×10^{-5}	3.1 x 10
Atmospheric DFe supply (mmol Fe m^{-2} d^{-1}) (1)	2.0×10^{-5}	2.5×10^{-5}	1.0×10^{-4}	1.7 x 10
Horizontal DFe supply (mmol Fe m^{-2} d^{-1})	0 (4)	0 (4)	3.9×10^{-4}	1.9 x 10
Total DFe supply (mmol Fe m^{-2} d^{-1})	1.3×10^{-4}	2.5×10^{-5}	5.5×10^{-4}	2.2 x 10
Total annual DFe supply (mmol Fe m^{-2})	4.7×10^{-2}	0.9×10^{-2}	20.0×10^{-2}	8.1 x 10
POC export 170 m (mmol C m^{-2} d^{-1})	3.2	1.7		
POC export 270 m (mmol C m^{-2} d^{-1})	3.9	1.4		
"Excess" C sequestration efficiency Ceffx 170 m (mol C mol^{-1} Fe)	13600	-	8640	154000
"Excess" C sequestration efficiency Ceffx 270 m (mol C mol^{-1} Fe)	23000	-		

(1) Guieu et al., (2018)
(2) Morris & Charrette, (2013)
(3) Blain et al., (2007) updated by Chever et al., (2010)
(4) The main flux is from below, lateral advection is likely negligible
(5) Pollard et al., (2009)